Development and evaluation of an advanced National Air Quality Forecast Capability using the NOAA Global Forecast System version 16

Patrick C. Campbell[1,2,*], Youhua Tang[1,2], Pius Lee[1], Barry Baker[1], Daniel Tong[1,2], Rick Saylor[1], Ariel Stein[1], Jianping Huang[3,4], Ho-Chun Huang[3,4], Edward Strobach[3,4], Jeff McQueen[3], Li Pan[3,4], Ivanka Stajner[3], Jamese Sims[5], Jose Tirado-Delgado[5,6], and Youngsun Jung[5], Fanglin Yang[3], Tanya L. Spero[7], and Robert C. Gilliam[7]

1. NOAA Air Resources Laboratory (ARL), College Park, MD, USA.
2. Center for Spatial Information Science and Systems, George Mason University, Fairfax, VA., USA.
3. NOAA National Centers for Environmental Prediction (NCEP), College Park, MD, USA.
4. I.M. Systems Group Inc., Rockville, MD, USA.
5. NOAA NWS/STI, USA.
6. Eastern Research Group, Inc (ERG), USA.
7. U.S. Environmental Protection Agency, Research Triangle Park, NC, USA.

*Corresponding Author: Patrick.C.Campbell@noaa.gov

Abstract

A new dynamical core, known as the Finite Volume Cubed-Sphere (FV3) and developed at both NASA and NOAA, is used in NOAA's Global Forecast System (GFS) and in limited area models (LAMs) for regional weather and air quality applications. NOAA has also upgraded the operational FV3GFS to version 16 (GFSv16), and includes a number of significant developmental advances to the model configuration, data assimilation, and underlying model physics, particularly for atmospheric composition to weather feedback. Concurrent with the GFSv16 upgrade, we couple the GFSv16 with the Community Multiscale Air Quality (CMAQ) model to form an advanced version of the National Air Quality Forecast Capability (NAQFC) that will continue to protect human and ecosystem health in the U.S. Here we describe the development of the FV3GFSv16 coupling with a "state-of-the-science" CMAQ model version 5.3.1. The GFS-CMAQ coupling is made possible by the seminal version of the NOAA-ARL Atmosphere-Chemistry Coupler

1

(NACC), which became the next operational NAQFC system (i.e., NACC-CMAQ) on July 20, 2021. NACC-CMAQ has a number of scientific advancements that include satellite-based data acquisition technology to improve land cover and soil characteristics, and inline wildfire smoke and dust predictions that are vital to predictions of fine particulate matter ($PM_{2.5}$) concentrations during hazardous events affecting society, ecosystems, and human health. The GFS-driven NACC-CMAQ model has significantly different meteorological and chemical predictions than the previous operational NAQFC, where evaluation of NACC-CMAQ shows generally improved near-surface ozone and $PM_{2.5}$ predictions and diurnal patterns, both of which are extended to a 72-hour (3-day) forecast with this system.

1. Introduction

Air quality is defined as the degree in which the ambient air is free of pollutants--which are either directly emitted into the atmosphere (primary air pollutants) or formed within the atmosphere itself (secondary air pollutants)--that cause degradation to human health, visibility, and/or ecological systems (WHO, 2005). Air quality is as ubiquitous and important as weather impacts, where outdoor air pollution is responsible for ~4.2 million early deaths globally each year (https://www.who.int/health-topics/air-pollution#tab=tab_1). To put this into perspective: this is over three times the number of people who die from HIV/AIDS and over eight times the number of homicides each year (2017 Global Burden of Disease Study: https://www.thelancet.com/gbd). Air pollution is costly, and leads to huge economic damage (Landrigan et al., 2018). There are also disproportionate impacts of air pollution across poorer people and some racial and ethnic groups, who are among those who often face higher exposure and potential responses to pollutants (Institute of Medicine, 1999; American Lung Association, 2001; O'Neil et al., 2003; Finkelstein et al., 2003; Zeka et al., 2006).

Air pollutants are composed of both gaseous and particulate species, which under prolonged exposure can cause non-carcinogenic (Lee et al., 2014) and/or carcinogenic adverse health effects (Demetirou and Vineis, 2015). High ground-level ozone (O_3) concentrations (i.e., smog) for example, can lead to decreased lung function and cause respiratory symptoms. These symptoms are particularly dangerous for sensitive groups such as young children, the elderly, and those with preexisting conditions that include asthma, chronic obstructive pulmonary disease (COPD), lung cancer, and respiratory infection (Kar Kurt et al., 2016).

To protect against the health and environmental impacts of air pollution, world agencies have developed regulations and standards on the allowable amount of primary and secondary air

82   pollution measured at different spatiotemporal scales (e.g., seconds to months and local to global

83   scales), which largely depend on the atmospheric lifetime of specific air components (WHO,

84   2005, 2010). Typically, the world's most extreme air pollution occurs near global megacities

85   where population density is highest (Marlier et al., 2016). Rapid economic growth in China, for

86   example has led to extremely high air pollution levels over the past decade (Zhou et al., 2017;

87   Liu and Wang, 2020), necessitating significant efforts to implement air pollution prevention and

88   control plans (Chinese State Council, 2013; Zhao et al., 2014). The U.S. Environmental

89   Protection Agency (EPA) defines ambient concentration limits for primary pollutants such as

90   sulfur dioxide (SO_2), oxides of nitrogen ($NO_x = NO+NO_2$), carbon monoxide (CO), lead (Pb),

91   and total (carbonaceous and non-carbonaceous) particulate matter (PM). Other important

92   primary pollutants include total volatile organic compounds (VOCs), which have many sources

93   (both natural and anthropogenic) and serve as vital precursor gases to secondary pollutants such

94   as ground-level O_3 and the formation of fine particulate matter with an aerodynamic diameter of

95   less than 2.5 μm ($PM_{2.5}$). Ground level O_3 and $PM_{2.5}$ are two of the six U.S. EPA "criteria

96   pollutants" that are regulated for their concentrations, exposure level, and health impacts. This is

97   largely because there is a relatively mature understanding of their sources, formation, and

98   characteristics (e.g., Sillman et al., 1990; Sillman 1995, 1999; Pinder et al., 2008; Kim et al.,

99   2011a, 2011b; Zhang et al., 2009a, 2009b; Campbell et al., 2015; Karamchandani, et al. 2017).

100   There is also a widespread ability to compare observed and simulated ambient ozone

101   concentrations over both short-term (McKeen et al., 2004, 2007, 2009) and dynamic long-term

102   periods (e.g., Astitha et al., 2017), which has helped lead to an understanding of their well-

103   attributable health impacts (e.g., WHO 2006, Sun et al., 2015; Zhang et al., 2018).

104   To address prolific air pollution concerns in the U.S. during the 1950s-1960s, the first

105 development and application of real-time air quality forecast (RT-AQF) models began in the

106 1970s-1980s (i.e., the 1st and 2nd generation air quality models) coincident with the

107 establishment of the U.S. EPA by President Nixon. Initially the models were based on empirical

108 approaches and statistical models (Zhang et al., 2012a); however, by the 1990s and early 2000s,

109 RT-AQF models underwent a significant evolution and evolved to more complex 3-D numerical

110 air quality models (3rd and 4th generation air quality models). These RT-AQF models involved

111 more sophisticated techniques including increasingly complex parameterizations and chemistry,

112 bias correction methods and data fusion, chemical data assimilation, and hybrid statistical or

113 numerical methods with artificial intelligence/machine learning algorithms to improve RT-AQF

114 model efficiency and predictions (Zhang et al., 2012b; Bai et al., 2018). RT-AQF models have

115 become vital tools to improve our understanding and prediction of how air pollutants form,

116 disperse, and deposit to the surface, and are used by local health and air managers to assess the

117 air quality conditions to make informed decisions on mitigation measures to reduce public

118 exposure.

119   To address the nation's need for reducing the adverse health effects of air pollution and

120 associated costly medical expenses, in 2002 Congress addressed the National Oceanic and

121 Atmospheric Administration (NOAA) to provide National AQF guidance (H.R. Energy Policy

122 Act of 2002 - Senate Amendment S. 517, SA1383, Forecasts and Warnings). A joint project

123 emerged from this amendment between NOAA and the EPA to develop and establish the initial

124 phase of a RT-AQF system, which consisted of the coupled NOAA's Eta meteorological model

125 (Black, 1994; Rogers et al., 1996) with EPA's Models-3 Community Multiscale Air Quality

126 (CMAQ) model (Byun and Ching, 1999; Byun and Schere, 2006). This "offline-coupled" model

127   provided O_3 forecast guidance for the northeastern U.S states (Kang et al., 2005; Otte et al.,

128   2005; Eder et al., 2006) and formed the early version of the National Air Quality Forecast

129   Capability (NAQFC) that was first implemented for operations in September 2004

130   (https://www.weather.gov/sti/stimodeling_airquality_predictions).   The NAQFC was further

131   developed at NOAA and collaborating laboratories (Mathur et al., 2008; McKeen et al., 2004,

132   2007, 2009), and was comprehensively evaluated in Eder et al. (2009). The NAQFC has been

133   continuously advanced to provide both O_3 and $PM_{2.5}$ forecast guidance for the entire

134   conterminous U.S. (CONUS), expanded its predictions to both Alaska and Hawaii, and provided

135   pivotal air quality forecast guidance to a multitude of stakeholders to help protect human health

136   and the environment (Stajner et al., 2011; Lee et al., 2017; Huang et al., 2017). Prior to the

137   advanced version described in this paper, the NAQFC used the offline-coupled North American

138   Mesoscale Model Forecast System on the B-Grid (NMMB) (Black, 1994; Janjic and Gall, 2012)

139   and CMAQv5.0.2 (U.S. EPA, 2014). The NAQFC provides forecast guidance for O_3, $PM_{2.5}$,

140   wildfire smoke, and dust at a horizontal grid spacing of 12 km over a domain centered on the

141   CONUS, Alaska, and Hawaii domains.

142   NOAA's National Weather Service (NWS) transitioned operationally in June 2019 to use a

143   new dynamical core known as the Finite Volume Cubed-Sphere (FV3) in the Global Forecast

144   System (GFS) model. Both the National Aeronautics and Space Administration (NASA) and

145   NOAA's Geophysical Fluid Dynamics Laboratory (GFDL; https://www.gfdl.noaa.gov/) have

146   developed and advanced FV3 over the past few decades (Lin et al., 1994; Lin and Rood, 1996;

147   Lin, 2004; Putman and Lin, 2007; Chen et al., 2013; Harris and Lin, 2013; Harris et al., 2016;

148   Zhou et al., 2019).   Overall, the switch to a FV3-based dynamical core with advancements to

149   GFS's observation quality control, data assimilation, and model physical parameterizations (from

150 the National Center for Environmental Prediction) significantly increases the accuracy of 1-2 day

151 and longer (e.g., 3-7 day) weather forecasts (Chen et al., 2019). Other advantages of FV3GFS

152 are improved computational efficiency and adaptable scaling, enhanced and flexible vertical

153 resolution, and improved representation of atmospheric circulation and weather patterns across

154 different horizontal scales (Yang et al., 2020;

155 https://www.weather.gov/media/notification/pns20-44gfs_v16.pdf;

156 https://www.emc.ncep.noaa.gov/emc/pages/numerical_forecast_systems/gfs.php;

157 https://ufscommunity.org/wp-

158 content/uploads/2020/10/UFS_Webnair_GFSv16_20201022_FanglinYang.pdf).

159 The improved representation of atmospheric conditions, circulation/transport, and

160 precipitation in GFS are pivotal to the accuracy of chemical predictions when coupled to RT-

161 AQF models. Since 2017, there also has been significant efforts at NOAA to use version 15 of

162 FV3GFS (hereafter, GFSv15) rather than NMMB as the meteorological driver for CMAQ in the

163 NAQFC (Huang et al., 2018, 2019, 2020). Huang et al. (2020) and Chen et al. (2021)

164 demonstrated that a version of the GFS-driven CMAQv5.0.2 (GFSv15-CMAQ) forecasting

165 system had partly improved O_3 predictions compared to the NMMB-driven CMAQ (NMMB-

166 CMAQ) system, but that the GFSv15-CMAQ had large biases for $PM_{2.5}$ that still need

167 improvement.

168 Concurrently at NOAA, there has been a major upgrade of GFS from version 15 to 16

169 (GFSv16), which includes a number of major developmental advances to the system (see Section

170 2 of this paper). Thus, there was an opportunity to simultaneously upgrade and streamline the

171 meteorological coupling between the GFSv16 and a more updated, "state-of-the-science" version

172 of CMAQ at the U.S. EPA (U.S. EPA, 2019; Appel et al., 2021). The current CMAQv5.0.2 used

173   in the NMMB-CMAQ and experimental GFSv15-CMAQ is outdated scientifically with

174   numerous deficiencies, many of which led to the elevated biases and error as described in Huang

175   et al. (2017; 2020) and Chen et al. (2021). Hence, there is a need to update the NAQFC to

176   actively developing versions of both FV3GFS and CMAQ.

177   The main objectives of this manuscript are to describe the development of the GFSv16

178   coupling with a state-of-the-science CMAQ model for the advanced updates to NAQFC that

179   includes numerous other RT-AQF science advances (Section 2). We also describe the new

180   simulation design and input observations, and evaluate the meteorological and air quality

181   predictions across the U.S. compared to the now discontinued NMMB-CMAQ system for

182   NAQFC (Sections 3 and 4). We conclude with a summary of NACC-CMAQ serving as the

183   current (since July 20, 2021) operational NAQFC, as well as longer-term goals (Section 5). We

184   hypothesize that advancing to closer state-of-the-science meteorological and chemical transport

185   models will improve atmospheric-chemical composition predictions, and the resulting air quality

186   forecasts will better protect human health across the U.S.

187   **2.   Methods**

189   2.1 Updated Meteorological and Surface Drivers

191   *2.1.1 The Global Forecast System Version 16*

193   The Environmental Modeling Center (EMC) at NOAA continuously develops and

194   improves the GFS model, which has been in operation at the National Weather Service since

195   1980. EMC has recently upgraded the GFS model from v15.3 to v16 in February 2021, and the

196   major upgrade improves the model forecast performance while also providing enhanced forecast

197   products. Some of the major structural changes to GFSv16 (compared to previous GFS versions)

198   include increased vertical layers/resolution from 64 to 127 (Figure 1) and an extended model top

199   from 54 (upper stratosphere) to 80 km (mesopause). GFSv16 also has a thinner first model layer

200   thickness (20 m) and higher resolution global horizontal grids of ~ 25 and 13 km (Yang et al.,

201   2020; https://www.weather.gov/media/notification/pns20-44gfs_v16.pdf;

202   https://www.emc.ncep.noaa.gov/emc/pages/numerical_forecast_systems/gfs.php;

203   https://ufscommunity.org/wp-

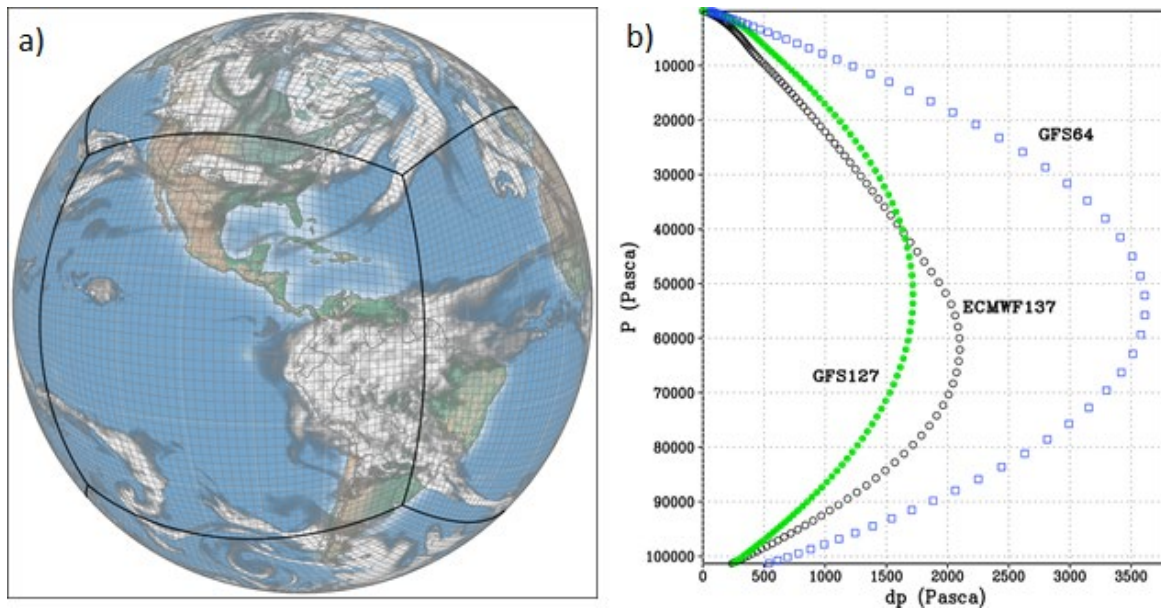204   content/uploads/2020/10/UFS_Webnair_GFSv16_20201022_FanglinYang.pdf).

206   **Figure 1.** The a) native FV3 gnomonic cubed-sphere grid at C48 (2-degree) resolution (image
207   courtesy of Dusan Jovic, NOAA) and b) vertical resolution (P vs. dP) for the upgraded GFSv16
208   (green) compared to the previous GFSv15.3 (blue) and the European Centre for Medium-Range
209   Weather Forecasts (ECMWF) model (black).
210
211
212   The GFSv16 has significantly improved its physical parameterizations (e.g., Planetary

213   Boundary Layer (PBL), gravity wave, radiation, clouds and precipitation, land surface, and

214   surface layer schemes) and upgraded to the Global Data Assimilation System (GDAS) Version

215   16 (Yang et al., 2020; https://www.weather.gov/media/notification/pns20-44gfs_v16.pdf;

216   https://www.emc.ncep.noaa.gov/emc/pages/numerical_forecast_systems/gfs.php;

217 https://ufscommunity.org/wp-

218 content/uploads/2020/10/UFS_Webnair_GFSv16_20201022_FanglinYang.pdf).

219   The global GFSv16 has changed format of forecast output history files from binary

220 (nemsio) to netCDF with zlib compression (data volume reduced by about 60%), and provides

221 the *hourly* (important for CMAQ predictions) output for a 72-hour (3-day) forecast each day.

222 The prior operational NAQFC (NMMB-CMAQ) forecast is only out to 48 hours (2-day). The

223 netCDF output is available (via live disk and archives) to all of NOAA's downstream model

224 applications, and is in the form of a Gaussian, rectangular grid with a global-uniform grid

225 resolution of ~13 km (referred to as "C768"), with a set number of latitude and longitude

226 coordinates. The NOAA GFDL website provides more information about FV3 and its grids

227 (https://www.gfdl.noaa.gov/fv3/). There are additional new surface fields in the GFSv16 output,

228 which include plant canopy surface water, surface temperature and moisture at four below-

229 ground levels (0-0.1, 0.1-0.4, 0.4-1, 1-2 m), surface roughness, soil and vegetation type, and

230 friction velocity.

231   *2.1.2 The NOAA-EPA Atmosphere Chemistry Coupler (NACC)*
232
233   The meteorological-chemical coupling of the GFSv16 to the regional, state-of-the-science

234 CMAQ *v5.3.1* model (U.S. EPA, 2019; Appel et al., 2021) is achieved via the NOAA-EPA

235 Atmosphere Chemistry Coupler (NACC) version 1 (NACC, i.e., *"knack": meaning an acquired*

236 *skill*), which is adapted from the U.S. EPA's Meteorology-Chemistry Interface Processor (MCIP)

237 version 5 (Otte and Pleim, 2010; https://github.com/USEPA/CMAQ). The NACC and CMAQ

238 coupling (hereafter referred to as NACC-CMAQ) involves a number of structural and scientific

239 advancements (Figure 2; "The Advanced NAQFC") compared to the previous operational

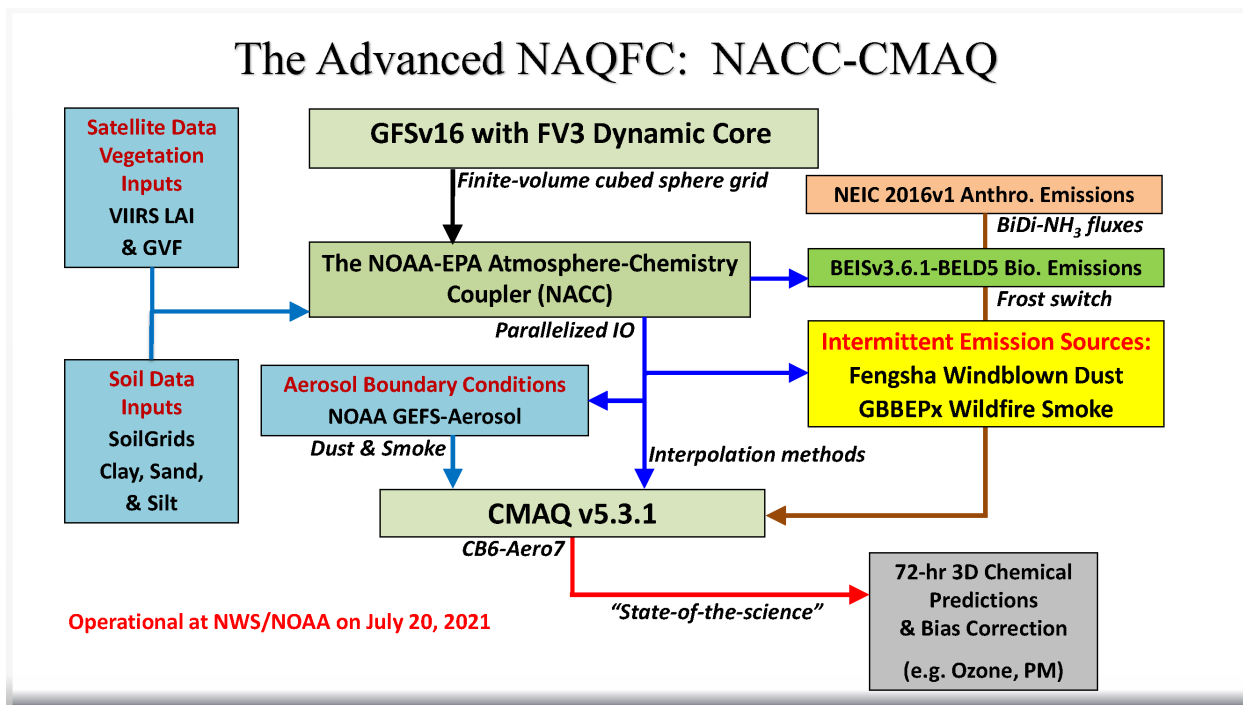240 NMMB-CMAQ; hereafter referred to as "prior NAQFC".

Figure 2. Schematic of the advanced NAQFC based on NACC-CMAQ.

The major structural changes to NACC-CMAQ include a variable-dependent bilinear or nearest-neighbor horizontal interpolation of the GFSv16 Gaussian gridded (~13 km) fields (e.g., 2-m temperature, 2-meter specific humidity, 10-m wind speed and direction, and sea level pressure) to Lambert Conic Conformal (LCC) at 12-km horizontal grid spacing (same as the prior NAQFC) (Figures 3a-b). NACC-CMAQ also includes a redefined vertical structure based on vertical interpolation (i.e., collapsing) to a 35-layer configuration (Figure 3c) that is identical to the prior NAQFC.
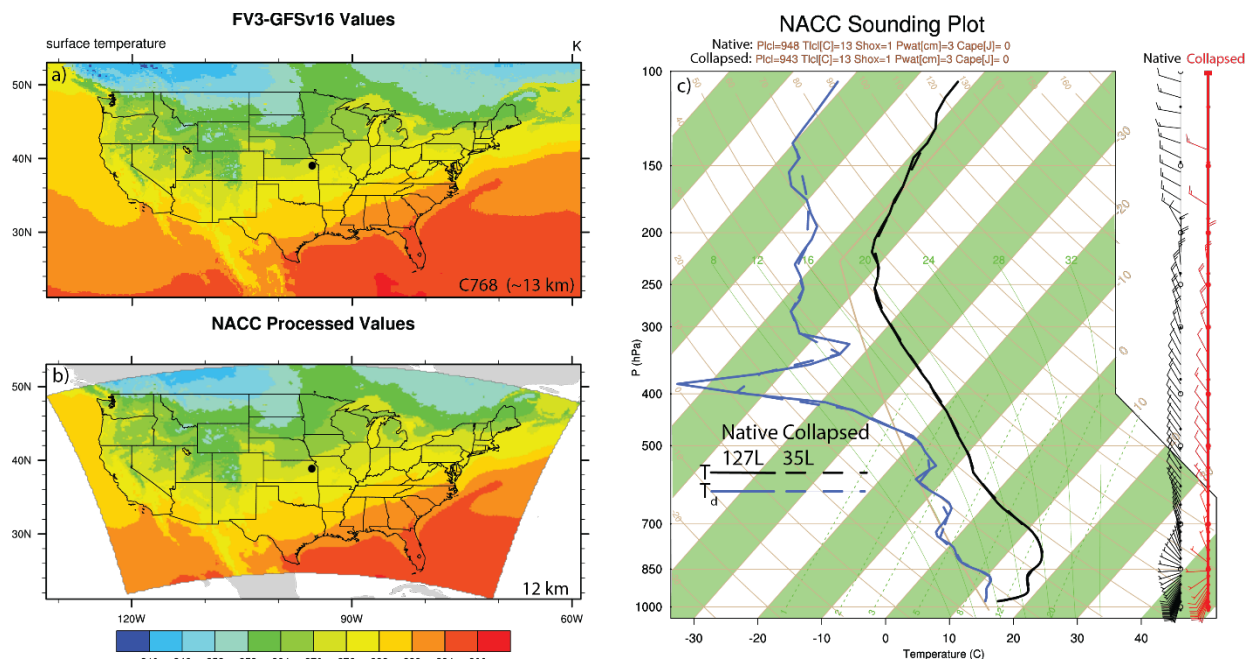
11

Figure 3. Examples of the NACC-CMAQ a) GFSv16 Gaussian grid surface temperature (C768~13 km) and b) associated bilinear horizontal interpolation NACC LCC output (12 km), and c) Skew-T Log-P diagram of both GFSv16 native (127 layers; solid) and NACC interpolated (35 layers; dashed) profiles of temperature (black) and dewpoint (blue), and wind speed/direction (wind barbs; native=black and collapsed=red). The example sounding pertains to a date of September 24, 2020 at the closest model grid square to 39.07°N and 95.62°W (black dot in a)-b)).

Time-splitting techniques based on Message Passing Interface (MPI) commands

parallelize the GFSv16-to-NACC input and output (IO), which vastly improves the

computational efficiency for the updated 72-hr forecast period.   The NACC-CMAQ coupling is

more unified and streamlined compared to prior NAQFC (Stajner et al., 2011; Lee et al., 2017;

Huang et al., 2017) and experimental GFSv15-CMAQ (Huang et al., 2018; 2019) applications,

while eliminating multiple pre- and post-processing steps.   The NACC-CMAQ processing steps

are therefore subject to less uncertainty/error that comes with multiple grid interpolations and

restructuring used previously, and are more computationally efficient for the 72-hr forecast

window. Furthermore, the vertical interpolation from 127 to 35 layers results in an excellent

agreement in the vertical structure of key atmospheric state variables (Figure 3c). While this

example is only for the central U.S., other model grid cell locations in the east and west U.S. also

12

271 demonstrate excellent agreement in the native and collapsed vertical structure in NACC (not

272 shown). While NACC-CMAQ domains for Alaska and Hawaii are also available for NAQFC,

273 this paper focuses only on the results inside the CONUS domain.

274   The left side of Figure 2 shows that NACC-CMAQ incorporates high resolution satellite

275 data for a 2018-2020 climatological (12-month) averaged leaf area index (LAI), which is based

276 on the Visible Infrared Imager Radiometer Suite (VIIRS) 8-day, Level 4 Global 500 m SIN Grid,

277 V001 product (Myneni and Knyazikhin, 2018; https://lpdaac.usgs.gov/products/vnp15a2hv001/).

278 This is a substantial update from the prior NAQFC, which assumed an unrealistic static value of

279 LAI = 4 across the entire domain. The NOAA product for near-real-time (NRT) greenness

280 vegetation fraction (GVF) from VIIRS (Ding and Zhu, 2018;

281 https://www.ospo.noaa.gov/Products/land/gvf/) is used as a dynamic, direct input in NACC-

282 CMAQ instead of using the GFSv16 vegetation fraction (VEG).   Both VIIRS LAI and GVF are

283 preprocessed, and NACC performs nearest-neighbor interpolation to the NAQFC grid.

284   More realistic land cover characteristics have shown to improve modeled meteorology,

285 chemistry, and surface-atmosphere exchange processes in the coupled Weather Research and

286 Forecasting (WRF; Powers et al., 2017; Skamarock & Klemp, 2008)-CMAQ model (e.g., Ran et

287 al., 2016; Campbell et al., 2019). Test results here show that rapid-refresh of high resolution

288 VIIRS LAI and GVF in NACC have distinct differences compared to an older 2010 MODIS-

289 International Geosphere-Biosphere Programme (IGBP) LAI climatology and GFSv16-based

290 VEG, respectively (Figs. S1-S2). The updated, dynamic LAI and GVF alter biogenic emissions,

291 dry deposition, and resulting concentrations of gases and aerosols in NACC-CMAQ, particularly

292 during the fall transition month of October 2020 (Fig. S3).

293   NACC-CMAQ also uses global, gridded soil information based on the 2019 SoilGrids[TM]

294   250-m resolution data (https://www.isric.org/explore/soilgrids) to drive an inline FENGSHA

295   Windblown dust model (Fu et al., 2014; Huang et al., 2015; Dong et al., 2016) in NACC-CMAQ

296   (Figure 2). Section 2.2 below provides more information on the specific parameters used in

297   FENGSHA.

298   As in the prior NAQFC, the chemical initial conditions (beginning on July 20, 2021 for

299   NACC-CMAQ) are taken from the previous day's (CMAQ) forecast output, and a NRT bias-

300   correction using AirNow surface observations (https://www.airnow.gov/) is applied to the 72-hr

301   predictions of O_3 and $PM_{2.5}$ (Figure 2). Huang et al. (2017) provides more information on the

302   bias-correction technique.

303   2.2 Updated Chemistry, Emissions, and Air-Surface Exchange Processes
304
305   *2.2.1 The Community Multiscale Air Quality (CMAQ) Model, Version 5.3.1*
306
307   A major update in NACC-CMAQ is coupling the GFSv16 to a "state-of-the-science"

308   chemical transport model, CMAQv5.3.1 (U.S. EPA, 2019; Appel et al., 2021) (Figure 2). The

309   prior NAQFC and experimental GFSv15-CMAQ both use CMAQv5.0.2, released in April 2014

310   (U.S. EPA, 2014). The major release of CMAQv5.3 incorporates significant improvements to

311   gas chemistry (e.g., halogen-mediated ozone loss), aerosol modules (e.g., improved secondary

312   organic aerosol formation), photolysis rates, aqueous and heterogeneous chemistry, transport

313   processes, air-surface exchange, emissions, and other structural and computational improvements

314   (Appel et al., 2021). The use of CMAQv5.3.1 in NACC-CMAQ also contains a number of bug

315   fixes to v5.3. Version 6 of the Carbon Bond (CB6) mechanism is used for gas-phase chemistry

316   (Yarwood et al., 2010), and the updated U.S. EPA's AERO7 module is used for aerosol

317   formation in NACC-CMAQ. The U.S. EPA's GitHub webpage

318   (https://github.com/USEPA/CMAQ/blob/master/DOCS/Release_Notes/README.md) contains

319   the CMAQv5.3 and v5.3.1 release notes, mechanism descriptions, and enhancements.

320   *2.2.2 National Emissions Inventory Collaborative (NEIC) 2016v1 Emissions*
321
322   The anthropogenic emissions modeling data may be the most influential input for chemical

323   transport model predictions in any AQF system (Matthias et al., 2018). The model emissions are

324   updated from National Emissions Inventory (NEI) 2014 version 2 that is used by the prior

325   NAQFC to NEI Collaborative (NEIC) 2016v1 Emissions Modeling Platform (NEIC, 2019),

326   which is based on updated models and datasets applied to the U.S. Environmental Protection

327   Agency's (EPA) NEI2014v2. The prior NAQFC uses an older NEI2014v2 emissions dataset.

328   There have been substantial updates to the NEIC2016v1, which include emission decreases for

329   CO, NO_x, SO_2, and $PM_{2.5}$, and increases in total VOC and ammonia (NH_3) emissions compared

330   to the NEI2014v2 (NEIC, 2019). The intermittent, "event-based" emissions from wildfires and

331   windblown dust, as well as persistent biogenic emissions sources are not from the NEIC2016v1,

332   but rather are dynamically predicted inline within NACC-CMAQ (described in following

333   sections). The NEIC2016v1 area-source (i.e., 2-D) emissions are gridded, netCDF/IOAPI format

334   that are interpolated to the 12-km NAQFC domain. The NEIC2016v1 also provides major point

335   source (i.e., 3D) emissions from six sectors: Commercial Marine Vehicles (CMV12 and

336   CMV3), Electricity Generating Units (EGUs), Non-EGUs, Oil-Gas sources, and "Other" point

337   sources. The anthropogenic point source plume rise is calculated inline within NACC-CMAQ

338   using the Briggs plume rise method (Briggs, 1965).   Slight adjustments are made to reduce the

339   anthropogenic aerosol/fugitive dust emissions over snow and wet soil surfaces to account for

340   different forecasted meteorology in GFSv16 compared to the conditions used in generating the

341   NEIC2016v1.

342   We note that the NEIC2016v1 emissions are not projected into the actual forecast year, with

343   the time lag being a long-recognized issue in NAQFC (e.g., Tong et al., 2012). Thus, the

344   NACC-CMAQ air quality simulations for the fall of 2020 and the winter of 2021 are impacted

345   by the COVID-19 pandemic, which resulted in spatiotemporal changes to emission patterns and

346   ozone formation over the U.S. in 2020 and beyond (Campbell et al., 2021). In addition, mobile

347   source emissions have continued to decline since 2016 so it is likely that the emissions used in

348   the analysis do not entirely reflect recent changes to the emissions compared to 2016 (almost 5

349   years earlier). We are actively working to improve the representativeness of anthropogenic

350   emissions sources in NACC-CMAQ and next-generation versions of the NAQFC.

351   *2.2.3 Inline Biogenic Emissions and Bidirectional NH$_3$ Fluxes*

352   NACC-CMAQ uses the latest version of the Biogenic Emission Inventory System (BEIS)

353   v3.6.1 (Vukovich and Pierce, 2002; Schwede, 2005) for estimating the biogenic VOC (BVOC)

354   emissions. BEISv3.6.1 includes updated vegetation inputs and advanced two-layer canopy

355   model formulations for estimating leaf (sun and shade) temperatures and vegetation data (Weiss

356   and Norman, 1985; Campbell and Norman, 1998; Niinemets et al., 2010; Bash et al., 2015).

357   NACC-CMAQ also uses the revised Biogenic Emissions Landuse Dataset v5 (BELD5), which

358   includes a newer version of the Forest Inventory and Analysis (FIA) version 8.0 and updated

359   agricultural land use from the 2017 U.S. Department of Agriculture (USDA) crop data layer.

360   The BELD5 dataset also uses a MODIS 21-category land use dataset with lakes identified

361   separately from oceans. The prior NAQFC used a much older BELD3 version.

362   The prior NAQFC also only considered summer factors in BEIS, and did not capture

363   seasonal (summer and winter) changes to the normalized biogenic emissions factors (vegetation

364   species-specific). NACC-CMAQ is improved and uses a new "vegetation frost switch" that

16

365   adjusts between summer and winter normalized emission factors in BEISv3.6.1 based on the

366   calendar date and 2-m temperature (TEMP2). In NACC, a new time-dependent variable,

367   'SEASON' is equal to one during the growing season, or equal to zero outside the growing

368   season. The SEASON is (boreal) summer if the calendar date is on or between 15 April and 15

369   October, but switches to winter if TEMP2 drops below 28°F, and is winter if the date is on or

370   between 16 October and 14 April, but switches to summer if TEMP2 rises above 32°F.   Thus,

371   the SEASON variable in NACC-CMAQ differs from typical retrospective CMAQ applications,

372   and is more dynamic with hourly variability based on the GFSv16 forecasted TEMP2. Test

373   results show generally improved model performance for all U.S. regions in December 2020

374   (winter) with vegetation frost switch compared to using only summer season normalized

375   emissions (Table S1). Using BELD5 further improves model performance and reduces the error

376   in all CONUS regions compared to the older BELD3 used in December 2020 tests (Table S1).

377   NACC-CMAQ includes bidirectional NH_3 (BIDI-NH_3) for NH_3 fluxes (i.e., both

378   deposition and evasion) in the CMAQv5.3.1 "M3Dry" deposition model (Nemitz et al., 2000;

379   Cooter et al., 2010; Massad et al., 2010; Pleim and Ran, 2011; Bash et al., 2010, 2013; Pleim et

380   al., 2013; 2019). Here, the NH_3 fertilizer emissions are removed from the base NEIC2016v1

381   inventory to avoid double counting, as the inline BIDI-NH_3 module calculates these fluxes. The

382   BIDI-NH_3 module typically requires daily inputs (e.g., soil ammonia content, soil pH, soil

383   moisture, and other soil characteristics) from the USDA's Environmental Policy Integrated

384   Climate (EPIC) agroecosystem model (https://epicapex.tamu.edu/epic/; Williams et al., 1995) to

385   calculate the soil ammonia concentrations that are combined with air concentrations in CMAQ to

386   calculate BIDI-NH_3 fluxes. Typically, the Fertilizer Emission Scenario Tool (FEST-C,

387   https://www.cmascenter.org/fest-c/) processes the necessary meteorological conditions for

17

388   integration with the EPIC simulation for input to CMAQ (Ran et al., 2011; Cooter et al., 2012).

389   Use of the EPIC/FEST-C system is not feasible in an NRT operational forecasting model, and

390   thus we use a pre-generated, full-year 2011 EPIC/FEST-C simulation based on Campbell et al.

391   (2019) for the daily inputs to BIDI-NH_3 in NACC-CMAQ. NACC-CMAQ directly uses the

392   GFSv16 soil moisture conditions in place of the FEST-C processed soil conditions required for

393   the latest version of BIDI-NH_3 in CMAQv5.3.1 (Pleim et al., 2019).

394   *2.2.4 Inline Wildfire Smoke and Windblown Dust Emissions*

395

396   Wildfires have been increasing in size (Westerling et al., 2006) and potentially in severity

397   (Miller et al., 2009) over the past decades. Wildfire smoke outbreaks can lead to extreme

398   concentrations of $PM_{2.5}$ and enhanced O_3, and are major concerns for air quality forecasting and

399   consequential human and ecosystem health impacts.   NACC-CMAQ includes a new inline

400   calculation of wildfire smoke emissions based on the Blended Global Biomass Burning

401   Emissions Product (GBBEPx V3; Zhang et al., 2012, 2014). GBBEPx provides daily global

402   biomass burning emissions ($PM_{2.5}$, BC, OC, NO_x, NH_3, CO, and SO_2). It blends fire

403   observations from two sensors, including the Moderate Resolution Imaging Spectroradiometer

404   (MODIS) on the NASA Terra and Aqua satellites, and the Visible Infrared Imaging

405   Spectrometer (VIIRS) on the Suomi National Polar-orbiting Partnership (SNPP) and Joint Polar-

406   orbiting Satellite System 1 (JPSS1) satellites. The GBBEPx data are further processed to prepare

407   model-ready emission datasets. First, the 0.1 x 0.1 degree latitude/longitude data are converted

408   into the NAQFC LCC projection.   U.S. EPA-based Sparse Matrix Operator Kernel Emissions

409   (SMOKE) fire speciation and diurnal profiles provide the PM speciation and diurnal patterns in

410   NACC-CMAQ, respectively, while both landuse and region are used to identify fire types.   The

411   fire duration persists for the 72-hour forecast period (with scaling of 1.0, 0.25, and 0.25 for day

412 1, 2, and 3, respectively) for wildfires identified when the grid cell forest fraction is > 0.4. In the

413 eastern U.S. (longitude east of 100°W), however, the fires are assumed to be mainly prescribed

414 burns in forested regions that only persist for the first 24-hours. The wildfire plume rise is

415 calculated inline within NACC-CMAQ using either the Briggs (1965) or Sofiev et al. (2012)

416 algorithms (Wilkins et al. 2019); currently the Briggs method is used by default.

417   Climate models project warming and drying trends in the southwestern U.S., where

418 intermittent windblown dust storms are becoming more frequent with the occurrence of drought

419 (Tong et al., 2017), or even "megadrought" conditions (Williams et al., 2020). Windblown dust

420 storms can lead to extreme levels of coarse mode particulate matter (i.e., PM_{10}), and cause

421 detrimental effects to human and agroecosystem health and visibility. NACC-CMAQ includes a

422 novel inline methodology for calculating windblown dust, based on the FENGSHA model

423 (Huang et al., 2015; Dong et al., 2016). In NACC-CMAQ, the potential for vertical dust flux in

424 FENGSHA is generally controlled by the sediment supply map (SSM), and the magnitude of the

425 friction velocity (USTAR) compared to a threshold friction velocity (UTHR) that determines the

426 USTAR needed to transfer dust from soil surfaces to the atmosphere. The UTHR is dependent on

427 the land cover and soil type, as well as the soil moisture. The SoilGrids^{TM} 250-m high-resolution

428 dataset (https://www.isric.org/explore/soilgrids) provides the necessary clay, silt, and sand

429 fractions used to calculate the SSM.

430 2.3 Updated Dynamic Aerosol Boundary Conditions
431
432   The chemical lateral boundary conditions (CLBCs) are critical to the prediction accuracy of

433 regional chemical transport models, particularly during intrusion events (Tang et al., 2009;

434 2021). The CLBCs represent the spatiotemporal distribution of chemical species along the

435 lateral boundaries of the domain of a regional model. NACC-CMAQ uses methods described in

436 Tang et al. (2021) and implements dynamic CLBCs (updated every 6-hours) for dust and smoke

437 aerosol data that are extracted (and mapped to CMAQ CB6-Aero7 species) from the NOAA

438 operational global atmospheric aerosol model, known as the Global Ensemble Forecast-Aerosols

439 (GEFS-Aerosols) member (Figure 2). GEFS-Aerosols is also based on the FV3GFS dynamical

440 core, which uses the Goddard Chemistry Aerosol Radiation and Transport (GOCART) model for

441 its sulfate, dust, BC, OC, and sea-salt aerosol predictions (Chin et al.; 2000; 2002; Ginoux et al.,

442 2001). GEFS-Aerosols uses the same wildfire smoke and windblown dust dataset/algorithms as

443 in NACC-CMAQ. The operational version of GEFS-Aerosols is run by the NWS as a special

444 unperturbed forecast of the Global Ensemble Forecast System version 12

445 (https://www.ncdc.noaa.gov/data-access/model-data/model-datasets/global-ensemble-forecast-

446 system-gefs), which provides an ensemble forecast product four times per day. Dynamic CLBCs

447 capture the signals of aerosol intrusion events such as biomass burning or windblown dust

448 plumes from outside the domain, which can improve the prediction accuracy of downstream O_3

449 and $PM_{2.5}$ concentrations at the surface (Tang et al., 2021).

450 **3. Simulation Design and Evaluation Protocol**

451

452 Table 1 summarizes the GFSv16/NACC-CMAQv5.3.1 model configuration described in

453 Section 2, as well as some additional model details. The model components and configurations

454 used in prior NAQFC system are summarized in Table S2 (based on Lee et al., 2017) for

455 comparison.

456 **Table 1. GFSv16/NACC-CMAQv5.3.1 model components and configurations.**

Model Attribute	Configuration	Reference
Domain	Contiguous U.S.; Center = 40°N;97°W	n/a
Horizontal Resolution	12 km	n/a

20

Vertical Resolution	35 Layers from near-surface to about 14 km (~ 60 hPa)	n/a
Meteorological ICs and BCs	FV3GFSv 16	https://nws.weather.gov/
Chemical ICs and BCs	2006 GEOS-Chem Simulation & GEFS-Aerosol Dynamic Smoke and Dust Aerosol CLBCs	http://acmg.seas.harvard.edu/geos/ *Tang et al.* (2021)
Anthropogenic Emissions	NEIC 2016v1 Platform	*NEIC* (2019)
Biogenic Emissions	Inline BEISv3.6.1 & BELD5	*Vukovich and Pierce* (2002)*; Schwede et al.* (2005)
Wildfire Emissions/Plume Rise	GBBEPxv3/ Inline Briggs	*https://www.ospo.noaa.gov/Products/land/gbbepx* *Briggs* (1965)
Microphysics	GFDL six-category cloud microphysics scheme	*Lin et al., 1983; Lord et al., 1984; Krueger et al., 1995; Chen and Lin, 2011; Chen and Lin, 2013*
PBL Physics Scheme	sa-TKE-EDMF	*Han and Bretherton (2019)*
Shallow/Deep Cumulus Parameterization	SAS Scheme	*Han et al. (2011; 2017)*
Shortwave and Longwave Radiation	RRTMg	*Mlawer et al. (1997); Clough et al.* (2005); *Iacono et al.* (2008)
Land Surface Model	Noah Land Surface Model	*Chen and Dudhia (2001), Ek et al. (2003), Tewari et al. (2004)*
Surface Layer	Monin-Obukhov	*Monin-Obukhov* (1954); *Grell et al.* (1994); *Jimenez et al.* (2012)
Gas-phase Chemistry	CB6	*Yarwood et al., 2010*
Aqueous-phase Chemistry	CMAQ AQCHem Updates	*Martin and Good* (1991)*; Alexander et al.* (2009); *Sarwar et al.* (2011)
Aerosol Module/Size	AERO7	*Appel et al.* (2021)
Other Model Attributes	-In-line Photolysis -In-line Bi-Directional NH_3 Exchange -In-line FENGSHA Wind-Blown Dust Emissions -In-line Sea-salt Emissions	*Binkowski et al.* (2007) *Nemitz et al., 2000; Cooter et al., 2010; Massad et al., 2010; Pleim and Ran, 2011; Bash et al., 2010, 2013; Pleim et al., 2013; 2019* *Fu et al., 2014; Huang et al., 2015; Dong et al., 2016*

		Kelley et al. (2010)

457

458   The simulation design consists of evaluations of one-month, continuous NACC-CMAQ

459   (72-hr, 3-day forecast) and prior NAQFC (48-hr, 2-day forecast) simulations for September 2020

460   (late summer/fall period) and January 2021 (winter period) (with previous 1-month spin-up and

461   training-data period) over CONUS at a horizontal grid spacing of 12 km (Table 1). September

462   2020 is used for the warm season because it is the closest month to summer when both the

463   NACC-CMAQ and prior operational NAQFC systems were simultaneously run. The prior

464   operational NAQFC was discontinued on July 20, 2021 due to computational constraints at

465   NWS/NOAA.

466   The Surface Weather Observations and Reports for Aviation Routine Weather Reports

467   (METAR), collected by NCEP's Meteorological Assimilation Data Ingest System (MADIS)

468   (https://madis.ncep.noaa.gov/madis_metar.shtml), provide observations of TEMP2, 2-m specific

469   humidity (Q2), and 10-m wind speed (WSPD10). The World Radiation Monitoring Center's

470   (WRMC's) Baseline Solar Radiation Network (BSRN) (https://

471   bsrn.awi.de/; Driemel et al., 2018) and U.S. Surface Radiation Network (SURFRAD;

472   https://gml.noaa.gov/grad/surfrad/) provide shortwave radiation observations at the ground

473   (SWDOWN). The PRISM Climate Group, Northwest Alliance for Computational Science and

474   Engineering, at Oregon State University (https://prism.oregonstate.edu/l; Accessed on 05 May

475   2021) provide gridded total precipitation observations (PRECIP). The National Oceanic and

476   Atmospheric Administration (NOAA), Earth System Research Laboratory's (ESRL's)

477   Radiosonde Database (RAOB) (https://ruc.noaa.gov/raobs/) provide vertical profile observations

478   of temperature, relative humidity, and wind speed. The U.S. EPA Air Quality System (AQS;

479 https://www.epa.gov/aqs) and near-real-time AirNow observational networks

480 (https://www.airnow.gov/) provide near-surface O_3 and $PM_{2.5}$ measurements.

481   The statistical measures used to evaluate the meteorological-chemical/air quality

482 predictions include the mean bias (MB), normalized mean bias (NMB), normalized mean error

483 (NME), Root Mean Square Error (RSME), Anomaly Correlation Coefficient (ACC), Pearson's

484 correlation coefficient (R), and Index of Agreement (IOA). Statistical measures such as R, NMB,

485 and NME provide measures of the associativity (i.e., correlation), bias, and accuracy,

486 respectively, of specific modeled surface and vertical meteorology and surface O_3 and $PM_{2.5}$.

487 The meteorological and chemical evaluations use the publicly available U.S. EPA Atmospheric

488 Model Evaluation Tool (AMET; Appel et al., 2011) and NOAA/ARL Model and Observation

489 Evaluation Toolkit (MONET; Baker et al., 2017).

490 **4. Results**

491

492 4.1 Meteorological Analysis

493

494   Compared to NMMB used in the prior NAQFC, the GFSv16 model has lower actual

495 TEMP2 in the east-southeast and parts of the northwest (Figures 4a-d), but has higher TEMP2 in

496 the central, northern plains, and parts of the west-southwest U.S. with higher 10-meter wind

497 speeds (WSPD10) in these regions (Figures 4i-l). GFSv16 is drier with widespread lower 2-

498 meter specific humidity (Q2; Figures 4e-h) and lower cloud fractions (CFRAC) (Figures 4m-p),

499 higher solar radiation absorbed at the ground (GSW; Figures 5a-d), lower longwave radiation

500 absorbed at the ground (GLW; Figures 5e-h), deeper planetary boundary layer height (PBLH;

501 Figures 5i-l), and generally more regions of increased precipitation (PRECIP; Figures 5m-p).

502 Differences in the CFRAC are (in part) impacted by differences in the model definition of cloud

503 cover; NMMB uses a binary cloud cover definition at each grid point, while GFSv16 uses

504   fractional cloud cover to calculate CFRAC. For stable conditions, the PBLH in the prior

505   NAQFC is re-diagnosed based on the Troen and Mahrt (1986) incremental calculation of the

506   bulk Richardson number (Ri_b) from the surface up to a height above the neutral buoyancy level

507   (i.e. approaching the critical Richardson number, Ri_{crit}) in the Asymmetric Convective Model v2

508   (ACM2) PBL scheme in CMAQ (Pleim 2007a;2007b). For unstable conditions, the re-

509   diagnosed ACM2 uses a slightly different PBLH formulation based on first finding the

510   convectively unstable mixing layer (z_{mix}), and then defining the point where $Ri_b = Ri_{crit}$ for the

511   entrainment layer above z_{mix}.   For both stable and unstable conditions, however, NACC-CMAQ

512   directly uses the diagnosed PBLH from the Turbulent Kinetic Energy (TKE)-based PBL scheme

513   in GFSv16 (Table 1; Han and Bretherton, 2019), which is also based on the Troen and Mahrt

514   (1986) incremental Ri_b formulation. Thus, NACC/GFSv16-CMAQ calculation is similar to the

515   re-diagnosed ACM2 PBLH for nighttime-stable conditions (with slight differences in Ri_{crit}

516   values), while there exists some distinct differences in their daytime-unstable PLBH

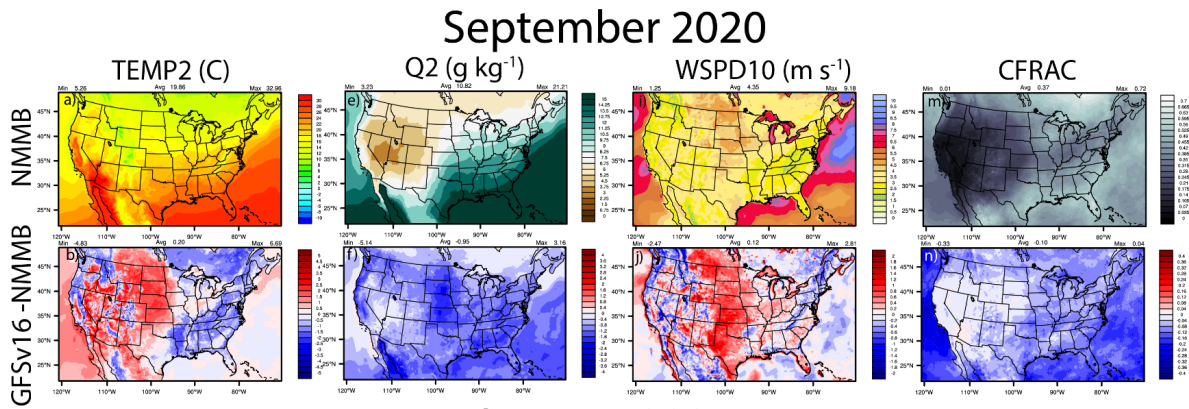517   formulations and Ri_{crit} calculations.
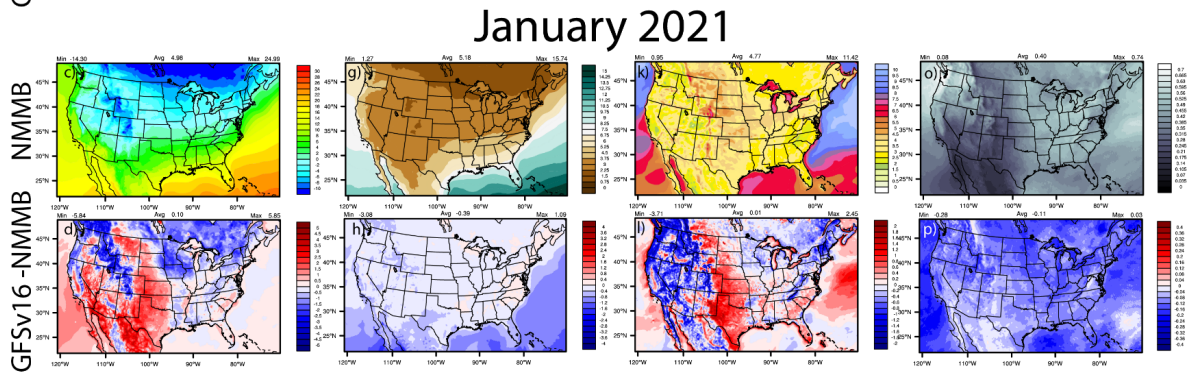
September 2020

Figure 4. September 2020 and January 2021 spatial average plots for NMMB (prior NAQFC) and the absolute differences for GFSv16 (NACC) - NMMB for TEMP2, Q2, WSPD10 and CFRAC.
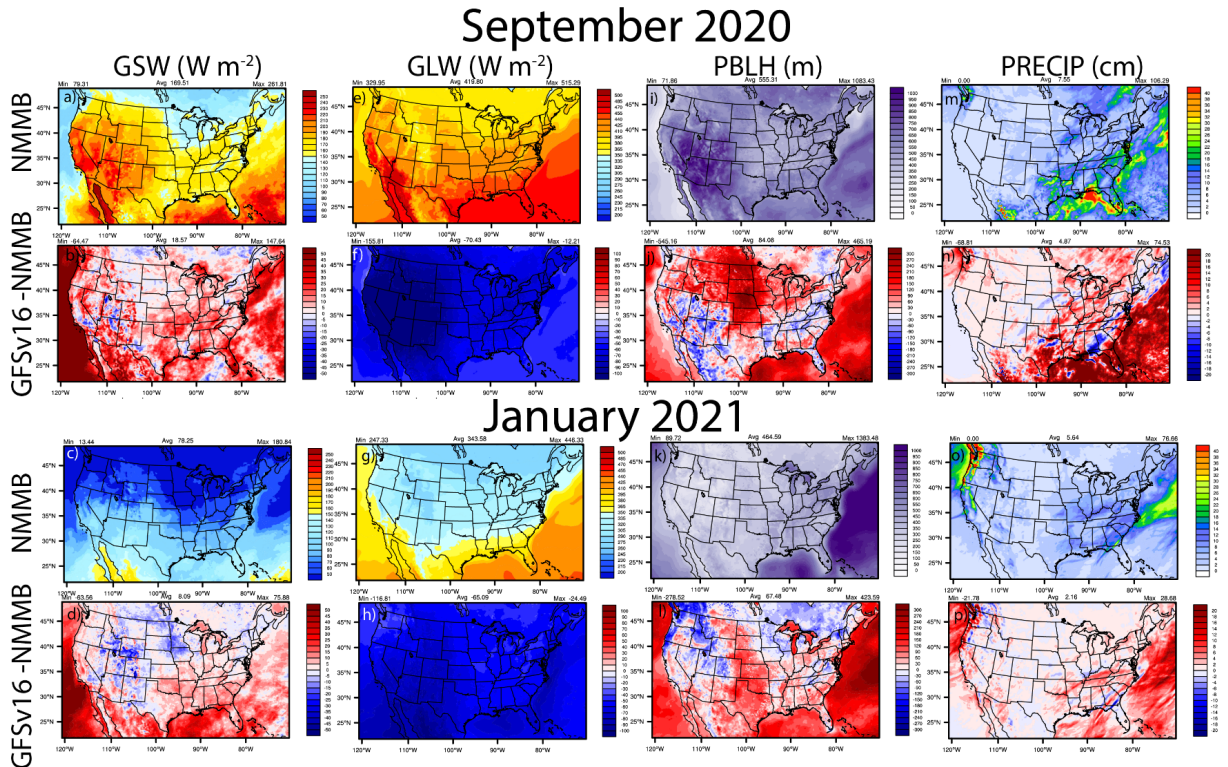
September 2020

Figure 5. Same as in Figure 4 but for GSW, GLW, PBLH, and PRECIP.

525   Consequently, the GFSv16 (NACC) and re-diagnosed ACM2 (prior NAQFC) diurnal PBLH

526   patterns are similar at night; however, the GFSv16 PBLH is considerably higher than the prior

527   NAQFC during the daytime for all regions in September and January (Supporting Figures S4-

528   S5).

529   The meteorological differences between GFSv16 and NMMB (Figures 4-5) influence

530   chemical predictions in CMAQ, which include a deeper daytime PBL and more precipitation that

531   can effectively dilute the gaseous and aerosol concentrations for NACC-CMAQ in some regions

532   across CONUS.   Areas of lower CFRAC and higher TEMP2 and GSW in GFSv16, however,

533   will increase photolysis and daytime O_3 formation in NACC-CMAQ in certain regions including

534   the south and upper Great Plains U.S. We note that although there are differences in the PBLH

535   calculation methodologies between the prior NAQFC and NACC-CMAQ (particularly for the

536   unstable daytime PBLH), the differences in near-surface meteorology (i.e., generally

537   warmer/drier) conditions in the GFSv16 (Table 2 and Table S2) also in part affect the differences

538   in PBLH (Figures 5i-l). These differences affect the pollutant mixing and dilution, and in part,

539   the resulting air quality predictions between the prior NAQFC and NACC-CMAQ (see Section

540   4.4 below).

541   4.2 Meteorological Evaluation and Metrics

542

543   Evaluation of the simulated day 1 (0-24 hr) forecasted meteorology against the METAR

544   network shows that GFSv16 generally has a higher positive TEMP2 (warmer) bias (Figure 6) in

545   the west, and has a CONUS-wide higher negative Q2 (dry) bias (Figure 7) compared to prior

546   NMMB (i.e., prior NAQFC) in both September and January.
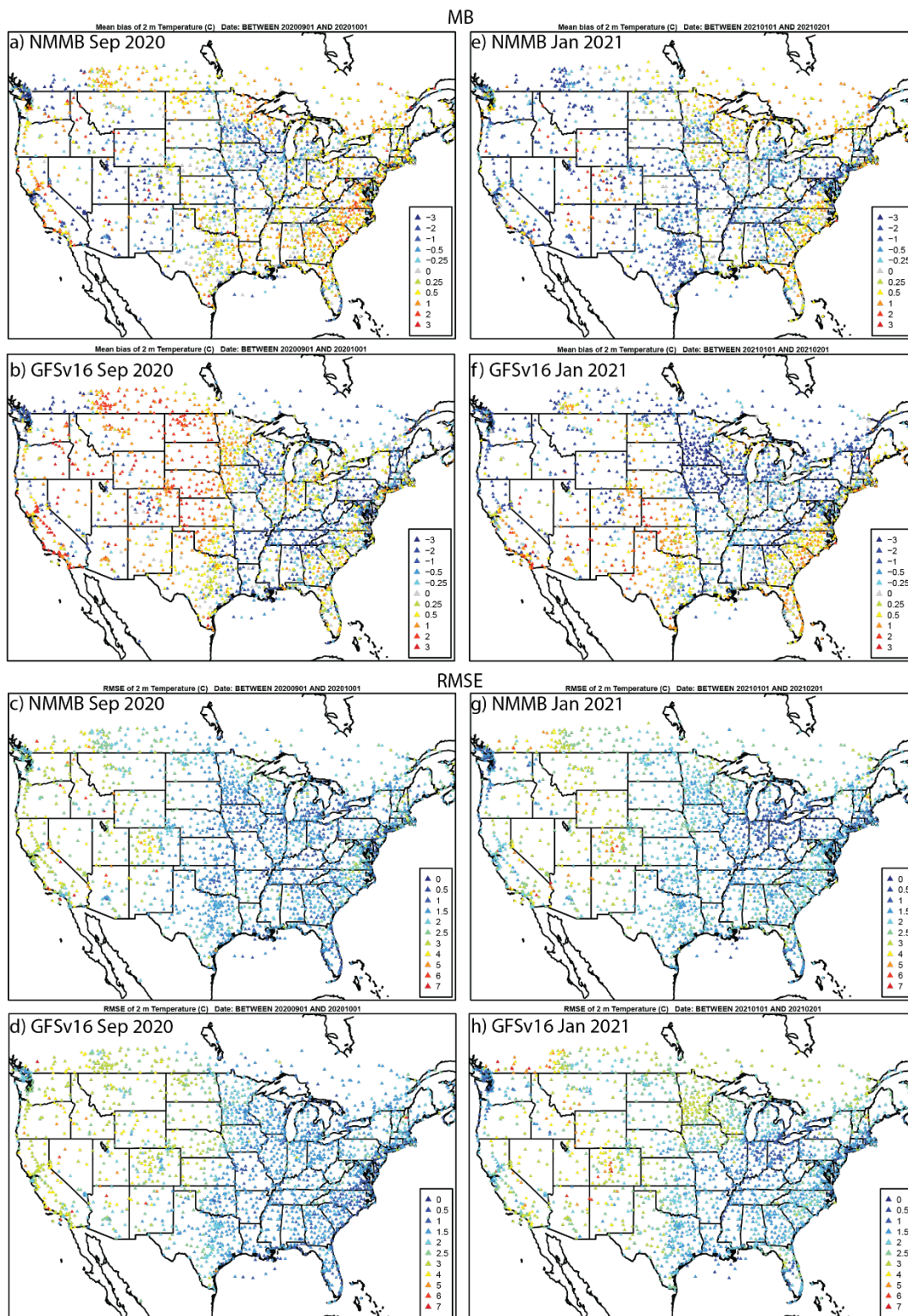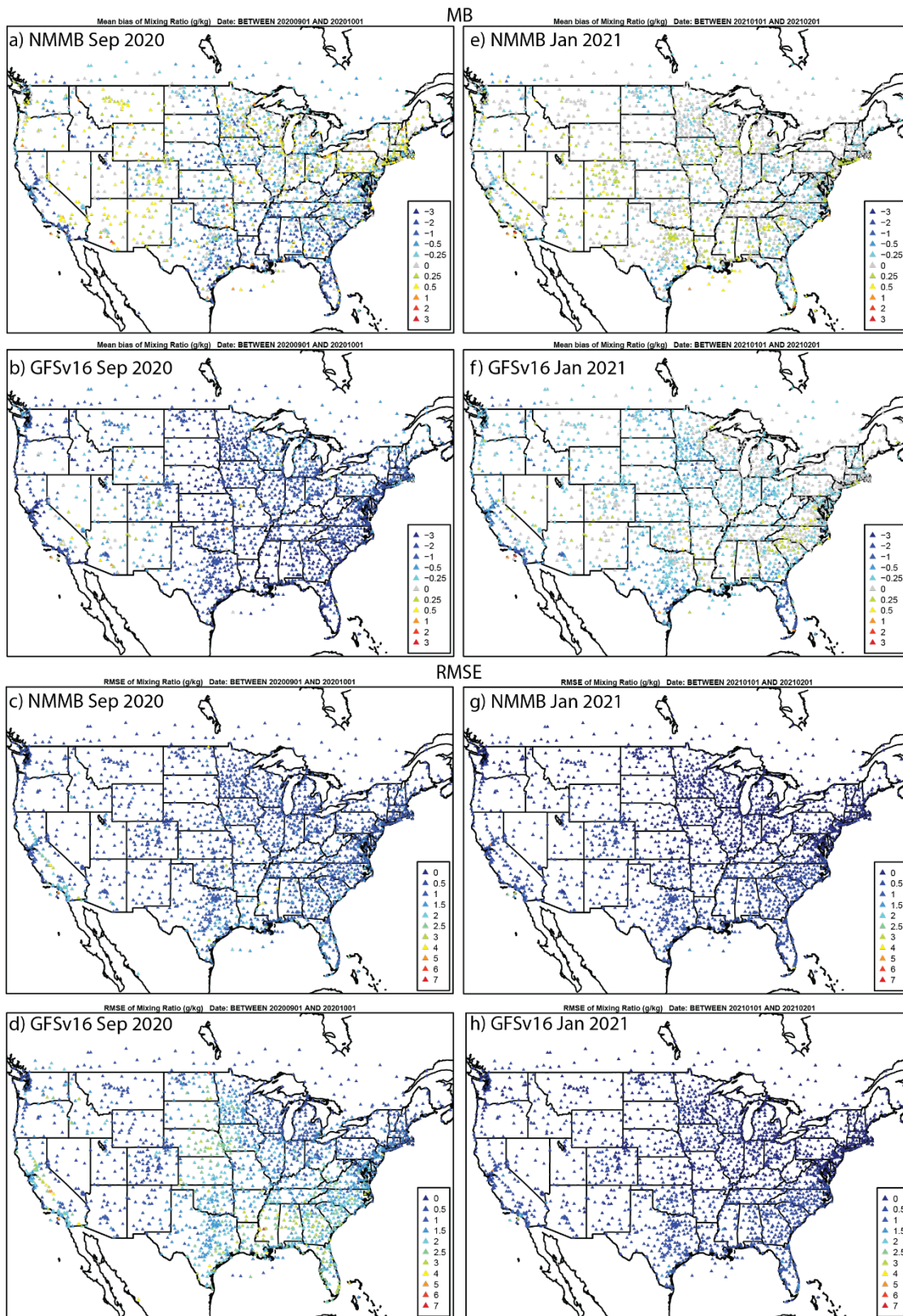
Figure 6. Average day 1 (0-24 hr) forecasted TEMP2 MB (°C) and RMSE (°C) for NMMB and GFSv16 during a)-d) September 2020 and e)-h) January 2021 compared to METAR observations.

Figure 7. Same as in Figure 6, but for Q2 (g kg^{-1}).

553   There are regions of higher RMSE for T2 and Q2, and lower/degraded ACC (Figures S7-S8) for

554   GFSv16 compared to NMMB, especially in the southern and western CONUS regions during

555   September.   The spatial patterns and magnitudes of WSPD10 bias and error are similar between

556   GFSv16 and NMMB (Figure 8); however, the higher WSPD10 for GFSv16 in the southern and

557   central CONUS leads to a shift from negative to positive biases from Texas northward to North

558   Dakota, especially during September. The WSPD10 RMSE is higher (Figure 8) and the ACC is

559   also lower/degraded (Figure S9) for GFSv16 in those regions, otherwise, the GFSv16 and

560   NMMB have similar performance for WSPD10. The day 1 forecast model performance (MB,

561   RMSE, and ACC) for 10-m wind direction (WDIR10) is similar between NMMB and GFSv16 in

562   both September and January (Figs. S6 and S10).
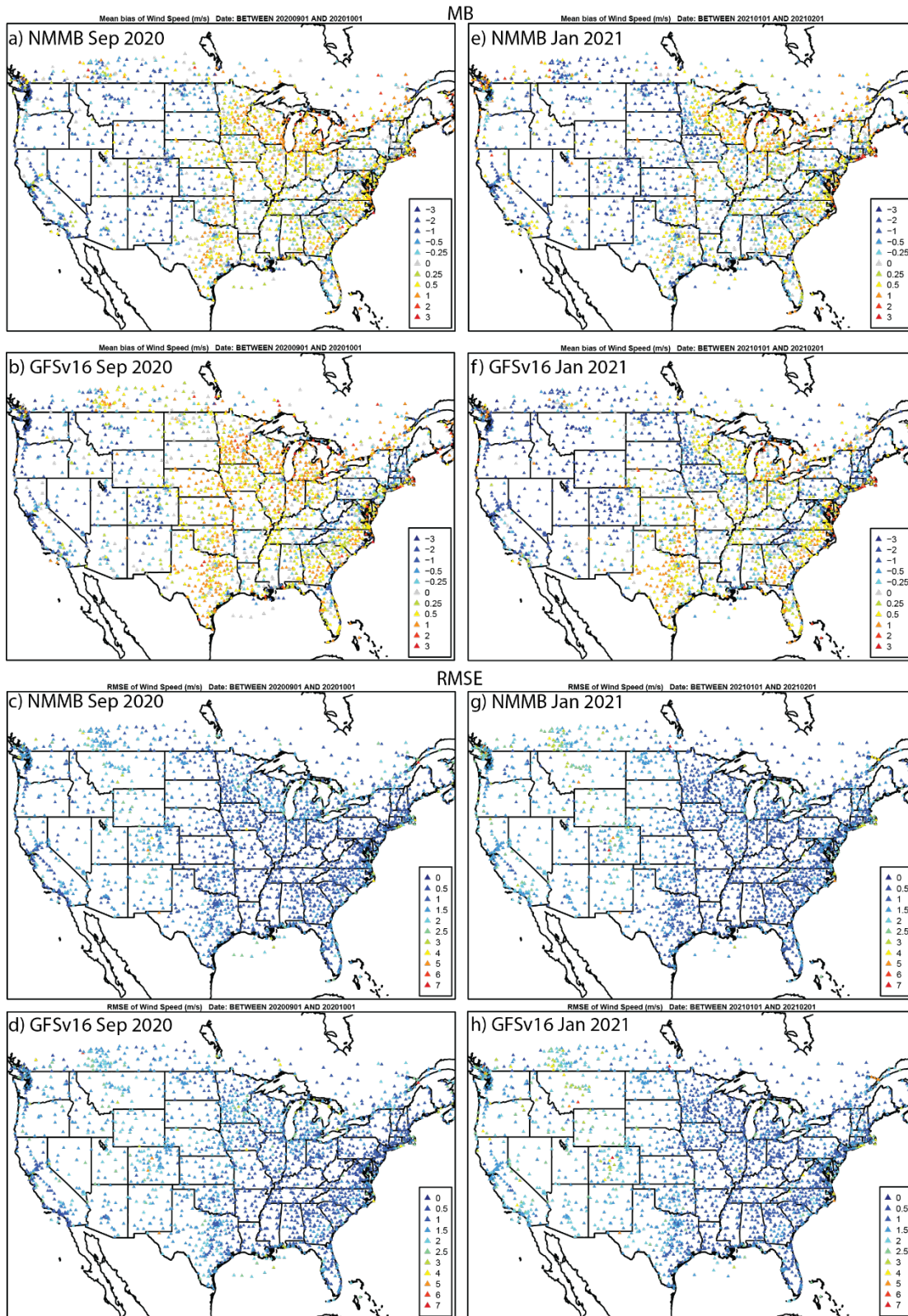
Figure 8. Same as in Figure 6, but for WSPD10 (m s^{-1}).

565   Overall, the GFSv16 results are favorable for driving the advanced NACC-CMAQ

566   system, with some areas of concern in the degraded TEMP2 and Q2 in the warmer/drier regions,

567   particularly in the south and west CONUS during September. This roughly correlates with

568   warmer/drier top-layer soil conditions in GFSv16 in these regions (Fig. S11), and thus land

569   surface/soil data assimilation and model improvement in GFSv16 is an active area of focus at

570   NOAA. The widespread dry bias in GFSv16 appears to be persistent, as an independent

571   evaluation of August 2019 demonstrated very similar spatial patterns and magnitude of Q2

572   underpredictions in the eastern half of CONUS compared to the METAR network (not shown).

573   The GFSv16-driven NACC-CMAQ system extends out to a 72-hour forecast. Hence,

574   there is a question of how the day 1 and 2 forecasts perform for NMMB vs. GFSv16 in the

575   eastern (<100° W) and western (>100° W) U.S., and how a day 3 forecast extension also affects

576   the GFSv16 diurnal and statistical model performance. The GFSv16/NACC diurnal patterns of

577   standard deviation, error, and bias for TEMP2, Q2, and WSPD10 are very similar to each other

578   for days 1-3 (Figures S12-14). While there is a slight increase in error and decreased correlation

579   (R), the relevant statistical metrics (e.g., MB, NMB, RMSE, and R) do not change appreciably

580   from day 1 to 3 for both September and January (Tables S3-S4). This lends confidence in the

581   utility of using the updated GFSv16 meteorology to drive a 72-hour air quality forecast in

582   NACC-CMAQ.

583   The day 1 diurnal statistics highlight both similar and contrasting TEMP2 and Q2

584   patterns for NMMB vs. GFSv16 in the eastern and western CONUS (Figures S12-S13). In

585   September (Figure S12a), NMMB has higher error and positive TEMP2 (i.e., warm) bias in

586   eastern CONUS during morning hours, and lower error with a slight cool bias in the

587   afternoon/evening, while GFSv16 shows slight overpredicted TEMP2 during most hours of the

588   day in the east. Over western CONUS, there are larger diurnal TEMP2 differences that include

589   small oscillating TEMP2 biases (about zero) for NMMB, along with distinctly large warm biases

590   during all daytime hours for GFSv16 in the west. There are larger error and negative Q2 (i.e.,

591   drier) biases for GFVSv16 compared to NMMB in eastern and western CONUS (Figure S13a).

592   In January, the TEMP2 and Q2 diurnal statistical patterns are similar for NMMB and GFSv16 in

593   both the eastern and western CONUS; however, the GFSv16 daytime hours have slightly higher

594   error and warmer and drier biases compared to NMMB (Figures S12b and S13b).

595   The total PRECIP is generally higher in GFSv16 compared to NMMB out East (Figure

596   5), which leads to larger overpredictions on average in CONUS compared to PRISM (Figure 9).

597   GFSv16 has a positive PRECIP bias on average in CONUS, NMMB has a negative bias, and

598   there is relatively more difference in the spatial patterns between NMMB and GFSv16 for

599   September compared to January. The difference is impacted by higher convective activity

600   during late summer/early fall in September compared to winter in January (not shown). Further

601   analysis indicated that generally heavier PRECIP in GFSv16 reduces the predicted $PM_{2.5}$

602   concentrations via wet deposition (not shown) in the east-southeast, and in parts of the west-
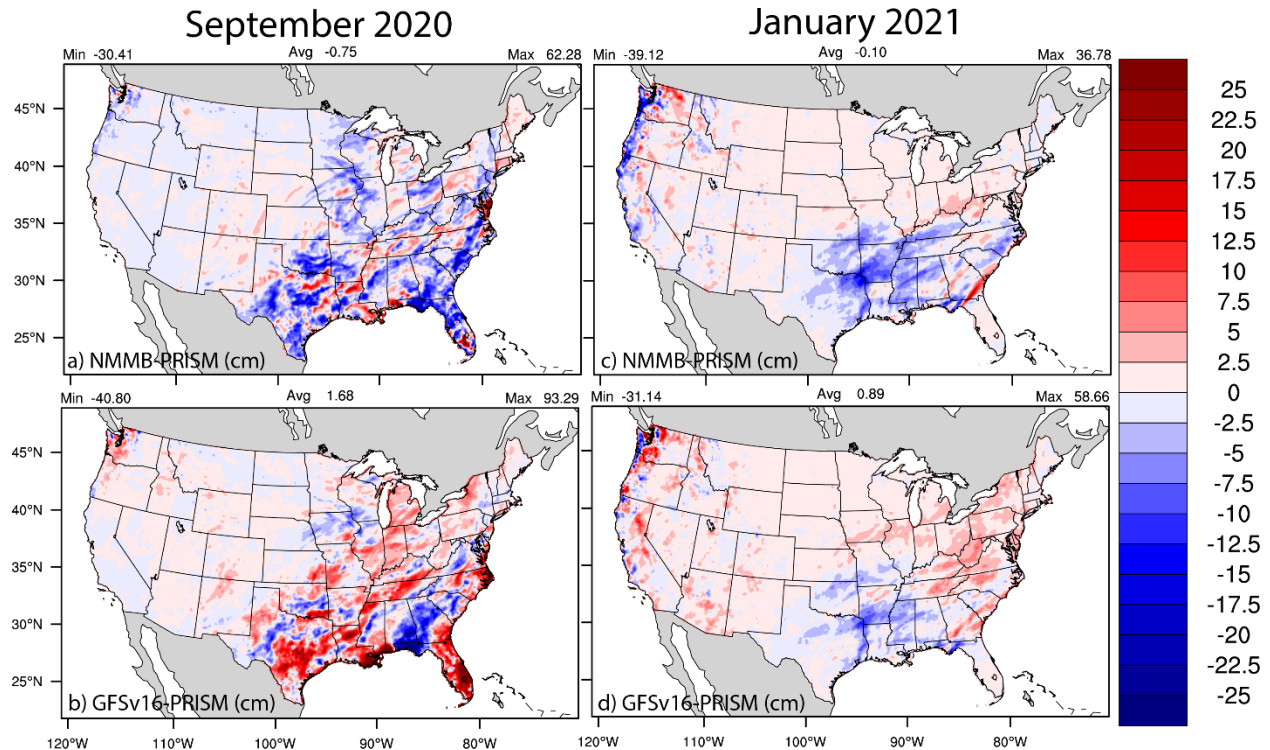
603   northwest compared to NMMB.

604

Figure 9. Average day 1 (0-24 hr) forecasted total PRECIP (cm) biases (Predicted-PRISM) for NMMB (top) and GFSv16 (bottom) during a)-b) September 2020 and c)-d) January 2021.

Comparisons of the model vertical profile statistics (i.e., MB, RMSE, and IOA) for TEMP, RH, and WSPD against an average of select RAOB observations across CONUS indicate that the GFSv16 (NACC) performs consistently with the operational NMMB (NAQFC) column (Figure 10; IOA nearly identical at ~ 0.8-0.9). GFSv16 is warmer and drier than NMMB in the model layers near the surface (> 850 mb), especially in September; however, GFSv16 has a moister atmospheric column with higher wind speeds compared to NMMB above the surface and in the free troposphere (< 850 mb). Figures S15-S17 show the spatial variability across the different RAOB sites used in the average for Figure 10. Analysis of the column (1000-250 hPa) average for all CONUS RAOB sites across CONUS indicate that GFSv16 has a predominantly cooler and moisture atmospheric column in September, despite being strongly warmer and drier near the surface (Figures S18-S19).
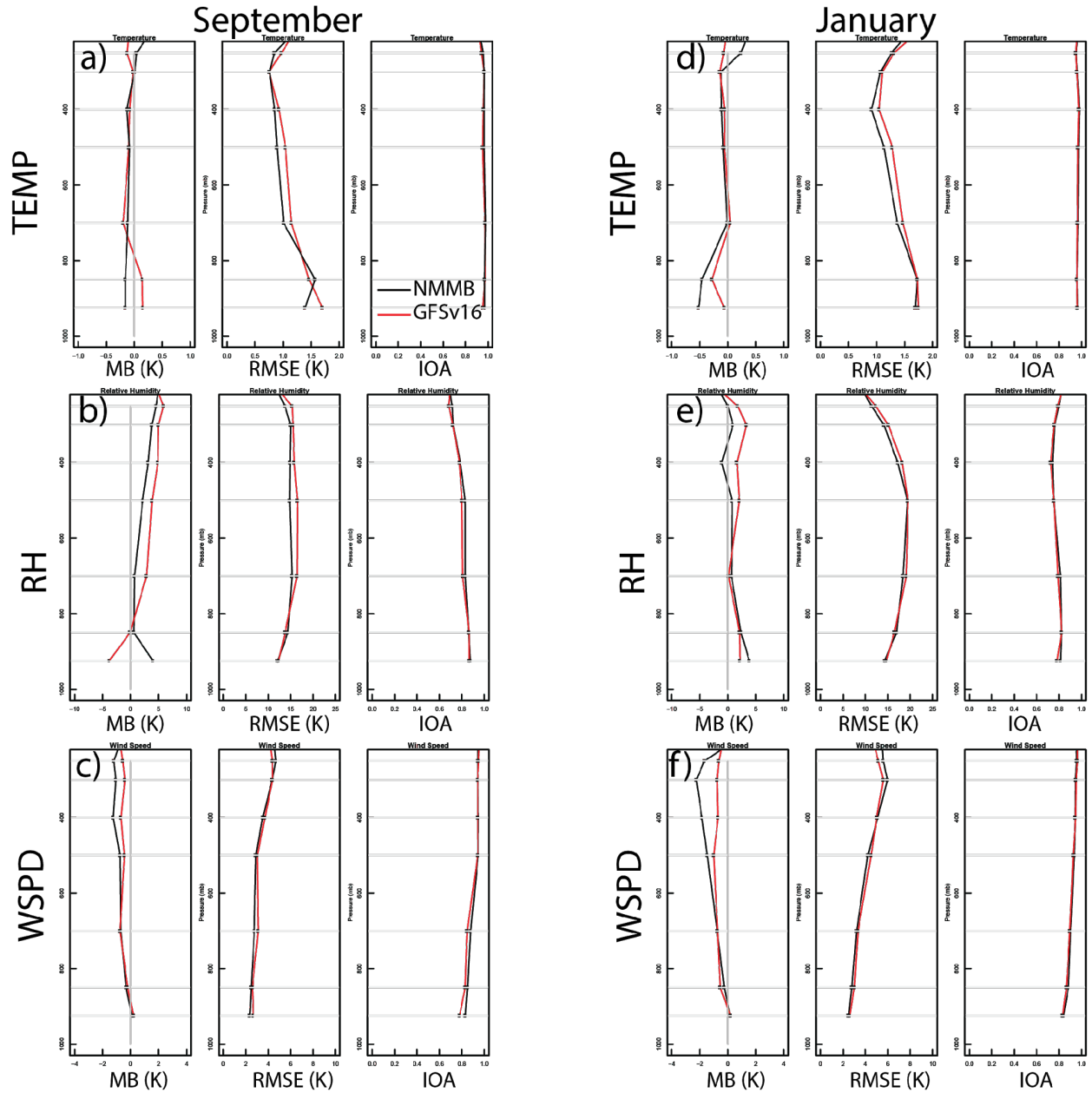
Figure 10. September 2020 (left) and January 2021 (right) vertical (1000 – 250 mb) temperature (TEMP), relative humidity (RH), and wind speed (WSPD) statistics (MB, RMSE, and IOA) for NMMB (black) and GFSv16 (red) against an average for select RAOB sites in CONUS. Supporting Figure S15a shows the specific RAOB site profiles, and Supporting Figures S18-S19 provides their relative locations.

4.3 Emissions Analysis

The updated NEIC2016v1 emissions in NACC-CMAQ are lower compared to the

NEI2014v2 emissions used in the operational NAQFC for all major species, except for NH_3

34

631   (Table 2), as the NEIC2016v1 includes updated data sources and model projections that

632   projected generally decreasing emissions compared to the NEI2014v2 (NEIC, 2019).

633   **Table 2.** September and January emissions totals (Tg) for the NAQFC CONUS domain.

Emission Species	NEI2014v2	NEIC2016v1	% Difference
September Total (Tg)			
CO	4.69	4.27	-8.9
NOx	0.92	0.75	-18.1
SO2	0.54	0.37	-31.2
NH3	0.48	0.59	23.9
AVOC	215.58	195.60	-9.3
POC	0.07	0.05	-26.8
PEC	0.03	0.02	-23.9
PMC	2.03	0.82	-59.3
January Total (Tg)			
CO	3.70	3.28	-11.2
NOx	0.78	0.64	-18.5
SO2	0.58	0.38	-34.7
NH3	0.10	0.12	18.4
AVOC	182.02	174.05	-4.4
POC	0.08	0.07	-10.8
PEC	0.02	0.02	-16.7
PMC	1.27	0.24	-80.8

634

635   The spatial emission changes show widespread decreases in the 2D area/mobile

636   emissions near the major urban cities for CO and NO_x and across the major interstates and

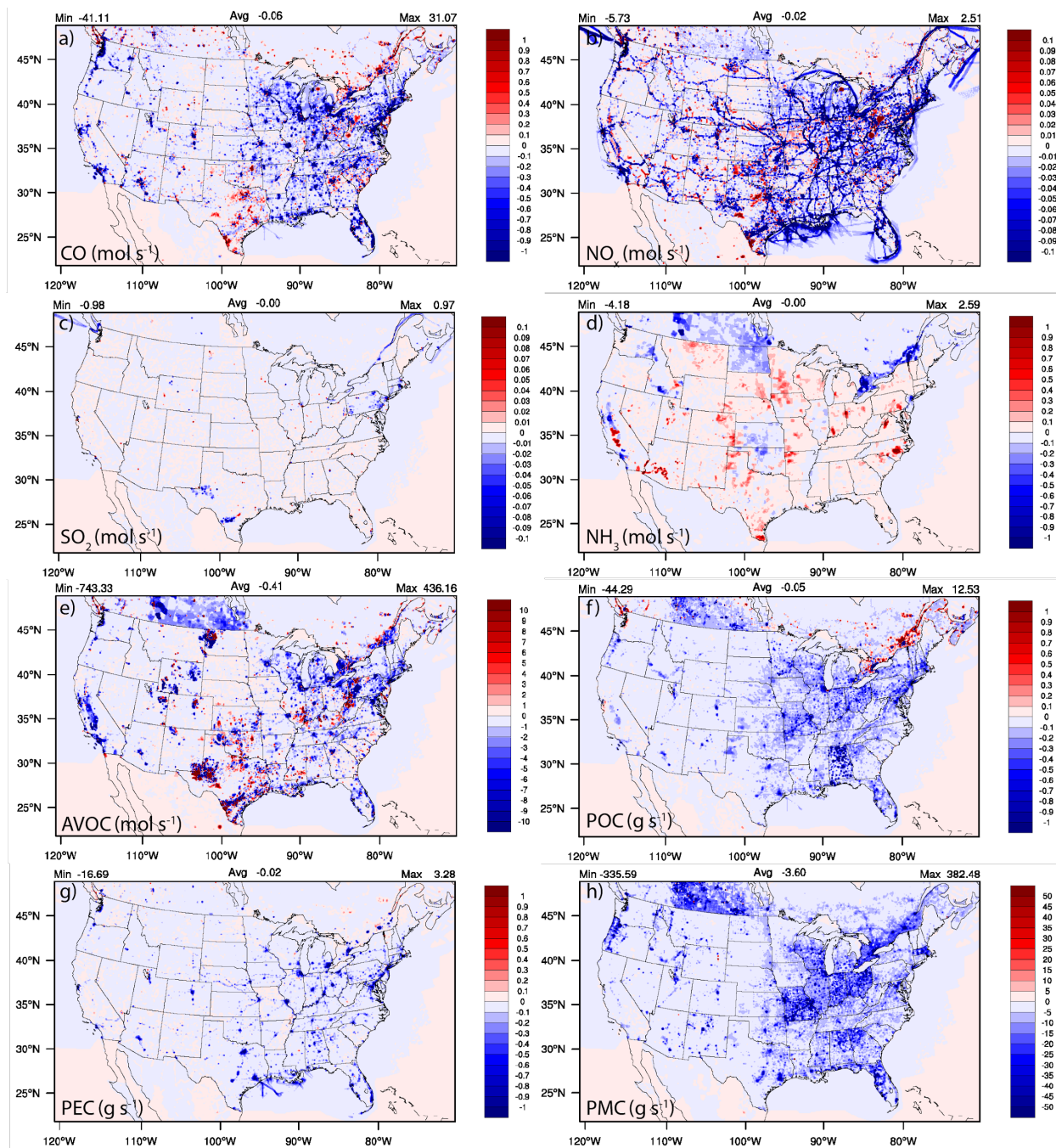637   railways for NO_x (Figures 11a-b).

638

Figure 11. September 2020 average spatial difference plots for NEIC2016v1-NEI2014v2 combined 2D area/mobile emissions. Figure S20 shows very similar emission changes for January 2021.

The spatial variability in NO_x emission changes, however, are impacted by changes in a number of onroad inputs including vehicles miles traveled, age distribution, and speeds, which caused some emissions to go up or go down depending on the specific counties. The NO_x emissions

647   variability is also impacted by national increases in railway levels and fuel use, while at the same

648   time being impacted by changes to fuel efficiency and cleaner engines for both passenger and

649   commuter trains. There are relatively minor area/mobile changes in SO_2 (Figure 11c), with some

650   exceptions in the east-northeast; however, there are widespread increases in NH_3 emissions

651   driven by changes to the livestock counts and updated fertilization methods and inputs found in

652   the NEIC2016v1 (Figure 11d).   Changes in nonpoint oil and gas production, exploration, and

653   emission factors generation, as well as changes to updated activity and data sources for

654   commercial cooking, residential fuel combustion, and industrial/commercial/institutional (ICI)

655   fuel combustion impact the AVOC area emission changes (Figure 11e). The widespread, and

656   spatially consistent decreases in POC and PMC are due to decreasing fugitive dust sources

657   (Figures 11f and 11h); with the exception of the St. Lawrence River Valley, that has both

658   increases in POC and AVOC (e.g., formaldehyde; not shown) emissions in the NEIC2016v1.

659   Updated appliance counts and residential wood combustion estimates affect the PEC area

660   emission decreases (Figure 11g).

661   There are also biogenic emissions differences due to the updated inline BEISv3.6.1 and

662   BELD5 in NACC-CMAQ (Table 2), and due to the impacts of NMMB (prior NAQFC) vs.

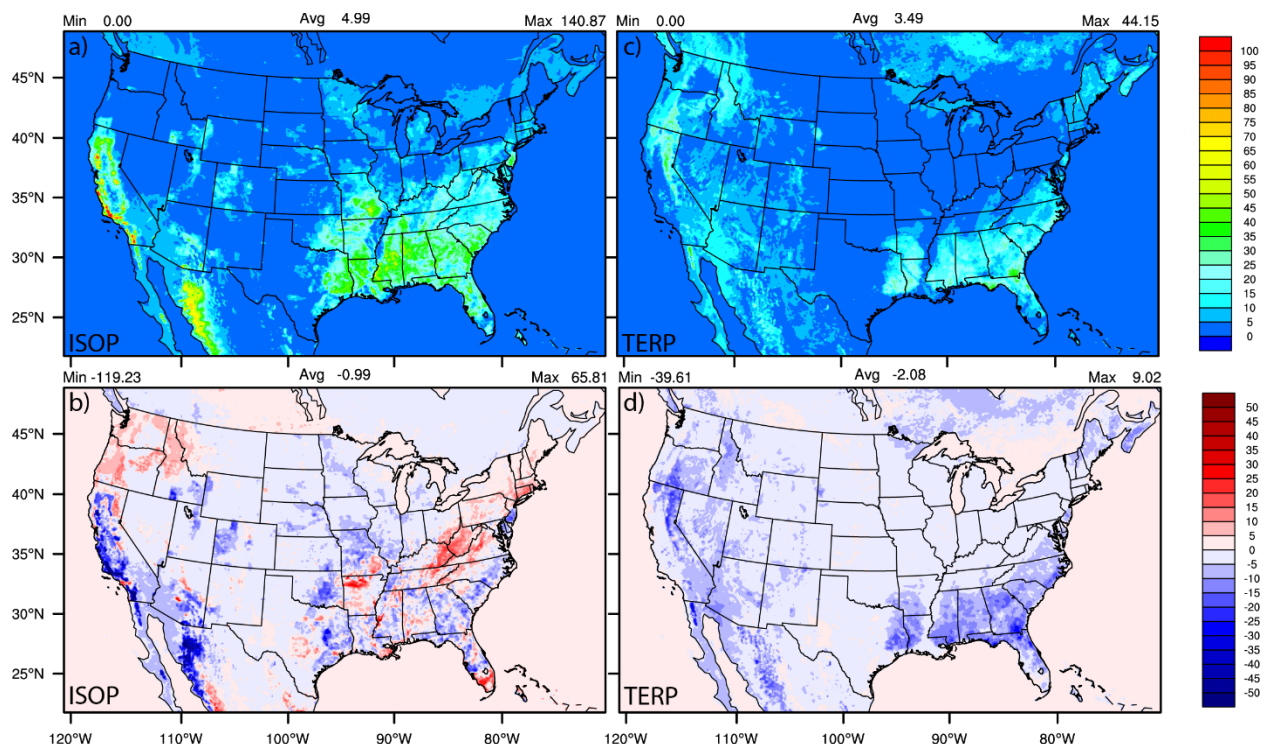663   GFSv16 (NACC) meteorology on BEIS calculations (Figure 12).

Figure 12. September 2020 average isoprene (ISOP) and terpene (TERP) emissions (top) in the prior NAQFC with BEISv3.1.4, and the absolute differences (bottom) for NACC-CMAQ (with BEISv3.6.1) - NAQFC.

The lower GFSv16 temperatures near many of the highly vegetated regions of the CONUS in September (Figure 4b) decrease the isoprene (ISOP) and terpene (TERP) emissions, with some notable, localized ISOP emission increases due to larger relative increases in downward solar radiation at the surface (GSW; Figure 5b) and resulting Photosynthetic Active Radiation (PAR; not shown). The differences are also impacted by the derivations of leaf temperatures in the updated BEISv3.6.1 and BELD5 in NACC-CMAQ compared to the BEISv3.14 and BELD3 in the prior NAQFC (see discussion in Section 2.2). Hence, the differences in spatial variability between ISOP and TERP emission changes stem from both differences in the locations of their relative maxima, and from the different algorithms for temperature and light dependencies in BEIS. The GFSv16 (NACC) performs very similarly to NMMB (prior NAQFC) for GSW at the surface compared against BSRN-SURFRAD observations in CONUS, with a slightly larger

680   overprediction in the late afternoon at some sites (Figures S21 and S22). The relatively lower

681   ISOP and TERP emissions in NACC-CMAQ will effectively lower the ground-level O_3 and

682   contribution of secondary organic aerosol (SOA) formation to $PM_{2.5}$ compared to the prior

683   NAQFC, particularly in the southeast and parts of the western CONUS in the late summer/early

684   fall. This is somewhat mitigated by enhanced GSW in NACC-CMAQ.

685   4.4 Air Quality Analysis
686
687   Here we focus on analysis of NACC-CMAQ predictions of gaseous O_3 for the late

688   summer/early fall (September 2020) and $PM_{2.5}$ concentrations during the winter (January 2021)

689   as concentrations are relatively higher for the pollutant's respective seasons. During the late

690   U.S. ozone season in September 2020, a large majority of the local NO_x concentration increases

691   in NACC-CMAQ (Figures 13a-b) correlate with areas of NO_x emissions increases in the

692   NEIC2016v1 compared to the NEI2014v2 (Figure 11b). An exception is the large NO_x increases

693   in the far west (e.g., California and Oregon) that stem from gaseous NO_x emissions from strong

694   wildfires that are captured by the GBBEPx in NACC-CMAQ (Table 1) but are excluded from

695   the prior NAQFC wildfire emissions system (Table S2).

696
697
698

September 2020 Gases
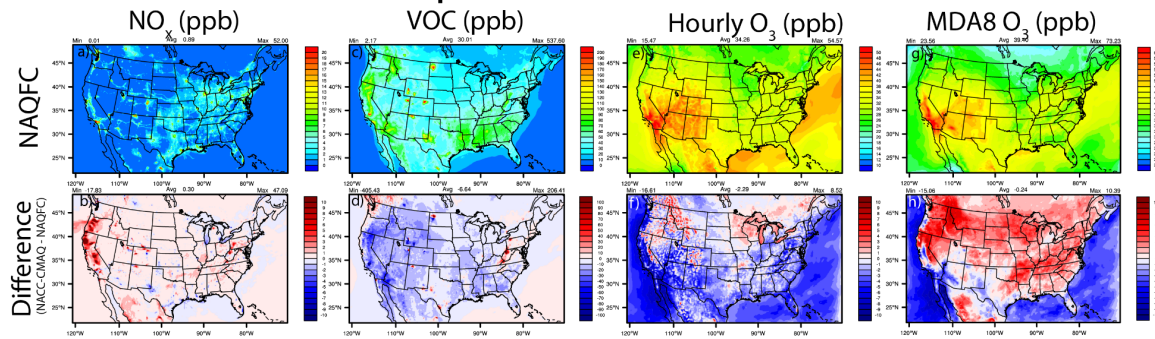
January 2021 Aerosols

699

703
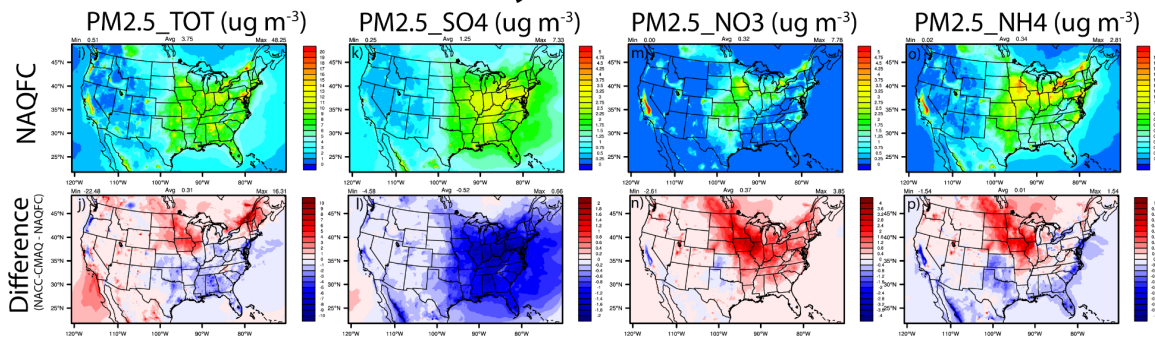
The increases in NO_x concentrations and enhanced nighttime O_3 titration, widespread decreases

in total VOC concentrations due to both anthropogenic and biogenic VOC emission decreases in

NACC-CMAQ, GFSv16-meteorology impacts (e.g., higher PBLH), and updated CMAQv5.3.1

chemistry/transport lead to widespread decreases in hourly O_3 when averaged over all hours

(Figures 13e-f). Regions of higher NO_x emissions, overall drier (i.e., widespread lower Q2)

conditions, and stronger mid- to late-afternoon solar radiation at the surface (i.e., widespread

higher GSW) (see Figures 4-5 and Figures S21-22) lead to enhanced daytime O_3 formation,

which is shown in the widespread increases in the maximum daily 8-hr average (MDA8) O_3 for

NACC-CMAQ (Figures 13g-h). This is particularly true for the strongly NO_x-limited conditions

across much of the western CONUS, where the MDA8 O_3 increases are impacted by large

increases in wildfire NO_x emissions in GBBEPx and VOC decreases (anthropogenic+biogenic,

40

715   but no wildfire VOC emission impacts) in NACC-CMAQ. These effects subsequently impact

716   the ozone NO_x-VOC sensitivity/regime that enhances the NO_x-saturated (i.e., VOC-limited)

717   conditions in this case (Figure S24). There are exceptions with MDA8 O_3 decreases in the west,

718   including western Oregon, the San Joaquin Valley in California, and regions of the southwest

719   CONUS, all of which are strongly VOC-limited (Figure S24). These regions are further

720   impacted by the VOC decreases and further NO_x saturation from wildfire emissions in some

721   locations of the west. Although outside the scope of this work, we also found that the

722   NACC/GFSv16-CMAQ system yields reasonable results when comparing fire-enhanced O_3 and

723    $PM_{2.5}$ concentrations to aircraft measurements during the 2019 Fire Influence on Regional to

724   Global Environments and Air Quality (FIREX-AQ) field campaign

725   (https://csl.noaa.gov/projects/firex-aq/) (not shown).   The widespread decreases in both the

726   hourly and MDA8 O_3 over all oceanic regions in the domain are driven by the updated halogen

727   (e.g., bromine and iodine chemistry) mediated O_3 loss in NACC-CMAQ, which can reduce

728   annual mean surface ozone over seawater by 25% (Sarwar et al., 2019).

729   There are both relatively large increases (north, northeast and west) and decreases (south-

730   southeast and parts of the west) for winter (January 2021) total $PM_{2.5}$ (PM25_TOT) in CONUS

731   for NACC-CMAQ compared to NAQFC (Figures 13i-j). The decreases in inorganic

732   PM25_TOT in the east-southeast are dominated by decreases in particulate sulfate (PM25_SO4)

733   and ammonium (PM25_NH4), while the increases in the north-central eastern CONUS are

734   driven by increases in particulate nitrate (PM25_NO3) and PM25_NH4. Further analysis

735   indicates that the widespread decreases in PM25_SO4, most prolifically in the east, are driven

736   strongly by widespread lower CFRAC in GFSv16 (Figure 4o-p) and lower aqueous-phase

737   oxidation in CMAQ (not shown). There are also contributions from decreased SO_2 emissions

41

738   found in some CONUS regions for NACC-CMAQ (e.g., northeast; Figure 11c). Additional

739   consumption of inorganic sulfate as secondary isoprene epoxydiol (IEPOX) organosulfates are

740   formed in the updated AERO7 aerosol mechanism in NACC-CMAQ (Table 1; Pye et al. 2013,

741   2017), and further contribute to the PM25_SO4 decreases. The higher total PRECIP for NACC-

742   CMAQ (Figure 5) also leads to lower PM25_TOT in the east-southeast regions.
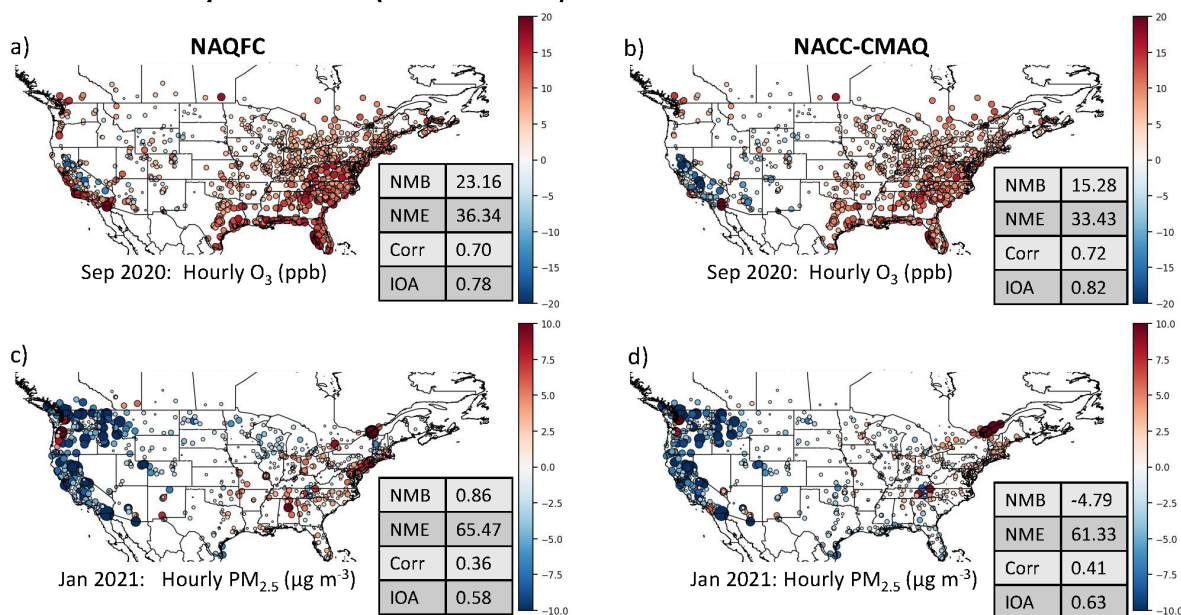
743   The largest PM25_TOT increases in the north-central CONUS are primarily driven by

744   enhanced ammonium nitrate formation, PM25_NO3 and PM25_NH4, which are influenced by

745   increases in NH3 emissions (Figure 11) and the inclusion of BIDI-NH3 fluxes in NACC-CMAQ

746   (Table 1). BIDI-NH3 in NACC-CMAQ allows for inline calculation of the diurnal pattern of

747   both NH3 evasion/emission and deposition, while the prior NAQFC only includes deposition.

748   Consequently, BIDI-NH3 in NACC-CMAQ generally increases ambient NH_4^+ and NO_3^- aerosol

749   concentrations (Bash et al., 2013; Pleim et al., 2019) compared to the prior NAQFC.

750   There are also contributions to the increased PM25_TOT from organic carbon sources

751   (Figure S25; PM25_OC), especially in the northeastern portion of the domain that include the St.

752   Lawrence River Valley region. This is in part due to enhanced anthropogenic VOC emissions in

753   NEIC2016v1 (Figure 11e, e.g., formaldehyde; not shown) and enhanced AERO7 secondary

754   organic aerosol formation in this region for NACC-CMAQ (not shown). There are also small

755   PM25_EC contributions to the PM25_TOT decreases in the east and increases in the west for

756   NACC-CMAQ (Figure S25), which are mainly due to decreases in anthropogenic PEC emissions

757   in the east (Figure 11g), but also from contributions of relatively small GBBEPx PM emissions

758   in the west (not shown). The prior NAQFC does not include biomass burning smoke emissions

759   during the month of January.

760

761   4.5 Air Quality Evaluations and Metrics

762

763   Evaluation of NACC-CMAQ shows overall improvement in the spatial MB of hourly O_3

764   (September) and $PM_{2.5}$ (January) against the AirNow network across CONUS (Figure 14).

765   There are clear reductions in the NAQFC overpreditions of O_3 and $PM_{2.5}$ in the east, and overall

766   reduction in NME, and overall improved correlation (R) and IOA for NACC-CMAQ. There are

767   also reduced overpredictions in the west for O_3 in September. The shifts to lower concentrations

768   result in larger domain-wide average $PM_{2.5}$ underpredictions for NACC-CMAQ compared to the

769   prior NAQFC (cf. Figure 13 above); however, *the improvements in R and IOA for NACC-*

770   *CMAQ are substantial*. The MDA8 O_3 spatial MB evaluation against AirNow behaves similarly

771   to NAQFC, with slight degradation in the model performance statistics because of areas of

772   higher overpredictions in the eastern U.S due to reasons discussed above for enhanced daytime

773   O_3 formation in NACC-CMAQ (Figure S26).

774
775
776

**Day 1 Mean Bias (Model-AirNow) Plots and Domain-Wide Statistics**

a) NAQFC

NMB	23.16
NME	36.34
Corr	0.70
IOA	0.78

Sep 2020: Hourly O_3 (ppb)

b) NACC-CMAQ

NMB	15.28
NME	33.43
Corr	0.72
IOA	0.82

Sep 2020: Hourly O_3 (ppb)

c)

NMB	0.86
NME	65.47
Corr	0.36
IOA	0.58

Jan 2021: Hourly $PM_{2.5}$ ($\mu g\ m^{-3}$)

d)

NMB	-4.79
NME	61.33
Corr	0.41
IOA	0.63

Jan 2021: Hourly $PM_{2.5}$ ($\mu g\ m^{-3}$)

777

782   The Day 2 forecasts have similar spatial model performance and statistics, with improved

783   hourly O_3 and $PM_{2.5}$ model performance (Figure S27) and slightly higher MDA8 O_3

784   overpredictions in the east for NACC-CMAQ (Figure S28). The consistent model performance

785   for Day 3 also shows utility in extending to 72-hr air quality forecasts in the advanced NACC-

786   CMAQ system (Figures S29-30). There is, however, a more notable degradation in skill for the

787   Day 3 forecast of $PM_{2.5}$ compared to O_3 in NACC-CMAQ (compare Figures 14 and S29).

788   There is significant improvement in the average O_3 and $PM_{2.5}$ diurnal patterns for each

789   CONUS region, other than higher daytime O_3 peaks for NACC-CMAQ compared to prior

790   NAQFC (Figure 15a-i). This is reflected in the improved R and IOA over CONUS on average

791   for NACC-CMAQ (Figure 14a-b). There is improved day-to-night O_3 transition, i.e., a sharper

792   slope or cutoff of daytime O_3 formation, which leads to lower nighttime O_3 mixing ratios in

793   NACC-CMAQ that agree better with AirNow observations for all CONUS regions.

794   The NACC-CMAQ $PM_{2.5}$ diurnal pattern also is more consistent with AirNow for most

795   CONUS regions (Figure 15j-s), which is supported by improved R and IOA (Figures 14c-d).

796   There are, however, some regions (e.g., northeast, south, and northwest) that the prior NAQFC

797   shows better diurnal performance in this case.

798
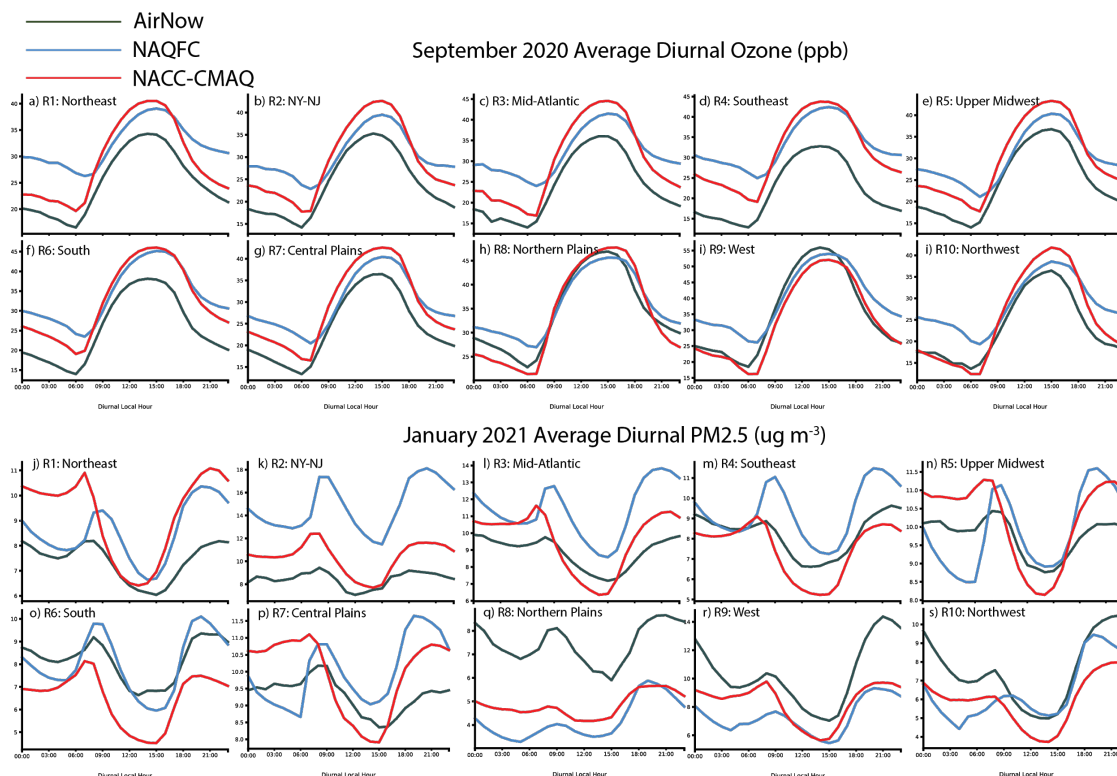
803   Overall performance evaluations of hourly O_3 in each CONUS region show

804   predominantly improved statistics for NACC-CMAQ, with increased R and IOA for all regions

805   (Table 3). Comparisons of the NMB, NME, and R against statistical benchmark values for

806   photochemical models based on Emery et al. (2017) indicate that both the prior NAQFC and

807   NACC-CMAQ are within specified criteria for hourly O_3 in most regions, except for relatively

808   large NMB values in the west and northwest regions. The increased hourly O_3 underpredictions

809   in NACC-CMAQ degrades the NMB to fail to meet the benchmark in the west, but improves the

810   NMB to fall within criteria in the northwest region.

811   **Table 3.** Average September 2020 hourly O_3 evaluation of the operational NAQFC and NACC-CMAQ
812   Day 1 forecasts against the AirNow network in different CONUS regions (based on
813   https://www.epa.gov/aboutepa/regional-and-geographic-offices).   Statistical benchmark values based on
814   Emery et al. (2017) are also shown for comparison. Following Emery et al., a >40 ppb (i.e., daytime)
815   cutoff for hourly O_3 is applied for the mean observations, mean models, mean bias, and the calculated
816   values of NMB and NME, but not for the correlation value (r) or index of agreement (IOA). Total # of
817   obs-model pairs are based on all values (i.e., no cutoff). **Bold** font indicates statistical values outside of
818   the Emery et al. criteria. *Italic* font indicates improved NACC-CMAQ performance. Supporting Tables
819   S5-S10 provide Day 2 and Day 3 (NACC-CMAQ only) forecast evaluations.

Day 1 Forecasts	Total # of Pairs	Mean Obs (ppb)	Mean Mod (ppb)	Mean Bias (ppb)	NMB (%)	NME (%)	Corr (r)	IOA
Benchmark Emery et al. (2017)	-	-	-	-	Goal: <±5% Criteria: <±15%	Goal: <15% Criteria: <25%	Goal: >0.75 Criteria: >0.50	-
Region 1 (Northeast)								
NAQFC	35983	46.85	43.55	-3.31	-7.06	15.04	0.61	0.71
NACC-CMAQ			43.44	-3.42	-7.29	15.14	*0.70*	*0.81*
Region 2 (NY-NJ)								
NAQFC	22944	46.68	42.90	-3.77	-8.09	17.88	0.59	0.72
NACC-CMAQ			45.18	*-1.50*	*-3.21*	*14.27*	*0.72*	*0.81*
Region 3 (Mid-Atlantic)								
NAQFC	89069	46.66	44.29	-2.37	-5.09	12.84	0.65	0.73
NACC-CMAQ			45.81	*-0.85*	*-1.83*	13.48	*0.74*	*0.82*
Region 4 (Southeast)								
NAQFC	105858	44.62	45.93	1.31	2.93	13.37	0.61	0.65
NACC-CMAQ			47.99	3.37	7.55	14.91	*0.74*	*0.75*

		Region 5 (Upper Midwest)						
NAQFC	109744	46.61	43.84	-2.77	-5.94	13.28	0.69	0.77
NACC-CMAQ			46.59	*-0.03*	*-0.05*	*10.69*	*0.77*	*0.83*
		Region 6 (South)						
NAQFC	84005	48.17	47.18	-0.99	-2.06	13.17	0.68	0.75
NACC-CMAQ			47.81	*-0.36*	*-0.75*	*12.80*	*0.75*	*0.81*
		Region 7 (Central Plains)						
NAQFC	27139	44.98	44.84	-0.14	-0.31	10.45	0.76	0.81
NACC-CMAQ			47.18	2.20	4.90	*9.54*	*0.82*	*0.86*
		Region 8 (Northern Plains)						
NAQFC	51759	48.97	44.64	-4.32	-8.83	13.89	0.71	0.82
NACC-CMAQ			45.08	*-3.89*	*-7.95*	14.00	*0.72*	*0.85*
		Region 9 (West)						
NAQFC	124051	55.44	50.29	-5.15	-9.29	18.37	0.69	0.79
NACC-CMAQ			46.37	-9.07	**-16.37**	21.78	*0.71*	*0.83*
		Region 10 (Northwest)						
NAQFC	14139	48.41	39.37	-9.03	**-18.66**	21.59	0.61	0.72
NACC-CMAQ			41.70	*-6.71*	*-13.86*	*19.91*	*0.66*	*0.81*

820

821   The higher MDA8 O_3 in NACC-CMAQ degrades its regional NMB, NME, and R

822 performance slightly compared to the prior NAQFC (Table 4), but R and IOA illustrate

823 improvements for most regions, in some cases substantially for R (e.g., northeast, southeast,

824 upper Midwest, and the Central Plains). The higher daytime O_3 overpredictions by NACC-

825 CMAQ in much of CONUS result in higher NMB and NME values that fall outside of the Emery

826 et al. (2017) benchmark criteria. These remain a concern for both the prior NAQFC and NACC-

827 CMAQ, and efforts are underway to address the persistent daytime O_3 overprediction in the

828 summer, particularly in the eastern U.S. (see Figures 14a-b and further discussion in Section 5).

829 **Table 4.** Same as in Table 3, but for MDA8 O_3. Note: As discussed in Emery et al. (2017),
830 cutoff values are not applied for MDA8 O_3.

Day 1 Forecasts	Total # of Pairs	Mean Obs (ppb)	Mean Mod (ppb)	Mean Bias (ppb)	NMB (%)	NME (%)	Corr (r)	IOA
Benchmark Emery et al. (2017)	-	-	-	-	Goal: <±5% Criteria: <±15%	Goal: <15% Criteria: <25%	Goal: >0.75 Criteria: >0.50	-
Region 1 (Northeast)								
NAQFC	1680	33.05	38.45	5.40	**16.35**	22.60	0.66	0.73
NACC-CMAQ			38.60	5.55	**16.81**	21.57	*0.73*	*0.75*
Region 2 (NY-NJ)								
NAQFC	1158	32.79	37.07	4.29	13.08	21.38	0.66	0.76
NACC-CMAQ			39.22	6.44	**19.63**	23.65	*0.74*	0.75
Region 3 (Mid-Atlantic)								
NAQFC	4243	33.85	39.35	5.50	**16.24**	20.75	0.74	0.77
NACC-CMAQ			41.31	7.46	**22.05**	24.54	*0.76*	0.75
Region 4 (Southeast)								
NAQFC	5076	31.01	40.30	9.29	**29.95**	**31.83**	0.64	0.64
NACC-CMAQ			41.06	10.05	**32.41**	**33.40**	*0.74*	*0.67*
Region 5 (Upper Midwest)								
NAQFC	5210	34.08	37.88	3.80	11.16	18.51	0.75	0.82
NACC-CMAQ			39.89	5.81	**17.06**	19.94	*0.82*	0.82
Region 6 (South)								
NAQFC	3901	35.65	42.37	6.72	**18.84**	23.91	0.74	0.77

NACC-CMAQ			43.01	7.35	**20.63**	24.35	*0.78*	*0.78*
Region 7 (Central Plains)								
NAQFC	1256	33.37	37.83	4.46	13.36	17.99	0.78	0.82
NACC-CMAQ			39.36	6.00	**17.97**	19.86	*0.85*	*0.84*
Region 8 (Northern Plains)								
NAQFC	2379	44.18	43.51	-0.47	-1.07	12.84	0.74	0.85
NACC-CMAQ			44.95	0.78	1.76	*11.78*	*0.79*	*0.88*
Region 9 (West)								
NAQFC	5757	51.03	51.26	0.23	0.44	17.84	0.70	0.82
NACC-CMAQ			48.03	-3.00	-5.88	18.73	0.68	0.79
Region 10 (Northwest)								
NAQFC	698	33.13	35.46	2.33	7.03	**25.11**	0.63	0.72
NACC-CMAQ			36.66	3.53	10.67	**25.58**	0.59	*0.74*

831

832

833   There are substantial improvements in the overall statistical $PM_{2.5}$ performance for

834 NACC-CMAQ, especially for R and IOA in most CONUS regions.   In many regions where the

835 prior NAQFC falls outside of photochemical criteria values (Emery et al., 2017), NACC-CMAQ

836 shows significant improvement to fall within the criteria. This demonstrates a substantial

837 improvement in the accuracy of the NACC-CMAQ system for $PM_{2.5}$ predictions (outside of

838 major wildfires), attributed to the scientific advancements described above.

839

840

841

842

843

844 **Table 5.** Same as in Table 3, but for 24-hr average PM2.5. Note: As discussed in Emery et al.
845 (2017), cutoff values are not applied for 24-hr average PM2.5.

Day 1 Forecasts	Total # of Pairs	Mean Obs (ppb)	Mean Mod (ppb)	Mean Bias (ppb)	NMB (%)	NME (%)	Corr (r)	IOA
Benchmark Emery et al. (2017)	-	-	-	-	Goal: <±10% Criteria: <±30%	Goal: <35% Criteria: <50%	Goal: >0.70 Criteria: >0.40	-
Region 1 (Northeast)								
NAQFC	1261	7.43	8.47	1.04	13.98	42.57	0.77	0.85
NACC-CMAQ			9.39	1.95	26.30	46.17	0.75	0.83
Region 2 (NY-NJ)								
NAQFC	598	8.54	15.39	6.85	**80.25**	**89.21**	0.72	0.55
NACC-CMAQ			10.84	*2.30*	*26.90*	*47.60*	*0.77*	*0.74*
Region 3 (Mid-Atlantic)								
NAQFC	1897	9.16	11.95	2.79	**30.43**	42.57	0.81	0.84
NACC-CMAQ			10.16	*1.00*	*10.96*	*33.24*	*0.83*	*0.89*
Region 4 (Southeast)								
NAQFC	3621	8.45	9.67	1.23	14.53	40.44	0.41	0.62
NACC-CMAQ			7.86	*-0.59*	*-6.98*	*37.19*	*0.48*	*0.67*
Region 5 (Upper Midwest)								
NAQFC	3270	9.61	9.79	0.19	1.93	38.09	0.58	0.75
NACC-CMAQ			9.65	*0.04*	*0.46*	*31.42*	*0.72*	*0.84*
Region 6 (South)								
NAQFC	2101	8.39	7.95	-0.44	-5.19	46.68	**0.28**	0.57
NACC-CMAQ			6.39	-2.00	-23.82	43.30	*0.36*	*0.59*
Region 7 (Central Plains)								

NAQFC	926	8.67	9.83	1.16	13.41	49.67	**0.32**	0.58
NACC-CMAQ			8.79	*0.12*	*1.40*	*32.13*	*0.68*	*0.82*
Region 8 (Northern Plains)								
NAQFC	1790	7.66	4.36	-3.30	**-43.13**	**60.51**	**0.33**	0.55
NACC-CMAQ			4.89	*-2.77*	*-36.20*	*52.68*	*0.49*	*0.67*
Region 9 (West)								
NAQFC	4118	10.09	7.04	-3.05	**-30.27**	46.97	0.61	0.74
NACC-CMAQ			7.98	*-2.11*	*-20.89*	**50.69**	0.56	0.73
Region 10 (Northwest)								
NAQFC	3922	7.93	6.86	-1.07	-13.54	**78.99**	**0.20**	0.46
NACC-CMAQ			6.33	-1.60	-20.19	*71.73*	*0.23*	*0.49*

846
847
848   The Day 2 forecast comparisons of the prior NAQFC and NACC-CMAQ regional

849 statistics are similar to Day 1, and that the Day 3 forecast extension for NACC-CMAQ has utility

850 with O_3 and $PM_{2.5}$ statistics predominantly falling within the benchmark criteria in most regions

851 (Tables S5-S10).

852 **5. Conclusions and Path Forward**

853   An advanced National Air Quality Forecasting Capability (NAQFC) was developed and

854 evaluated, using NOAA's FV3-based Global Forecast System (GFS) as the driving meteorology

855 for a state-of-the-science Community Multiscale Air Quality (CMAQ) model, version 5.3.1. A

856 key component of this new system is the development of the NOAA-EPA Atmosphere

857 Chemistry Coupler (NACC), which forms the bridge between the GFSv16 meteorological fields

858 and the CMAQ inputs for improved chemical predictions (i.e., NACC-CMAQ).   Such

859 advancements of the NACC-CMAQ system include high-resolution satellite vegetation inputs,

860 with a rapid-refresh VIIRS greenness vegetation fraction and VIIRS climatological leaf area

861   index, as well as additional soil data inputs to an improved windblown dust (FENGSHA)

862   algorithm in CMAQ. The anthropogenic, biogenic, and wildfire emissions in NACC-CMAQ are

863   also updated compared to the prior NAQFC, and for the first time, the forecasting model

864   calculates inline bidirectional NH_3 fluxes. NACC-CMAQ also ingests novel smoke and dust

865   aerosols at its lateral boundaries dynamically from the NOAA operational GEFS-Aerosols

866   model. Finally, the NACC-CMAQ system extends the air quality forecast from 48 to 72-hours,

867   and provides scientific advances in atmospheric chemistry modeling to state and local forecasters

868   out to 3 days. The additional day of forecast guidance could aid decision makers to prepare

869   citizens for localized air quality conditions that could adversely affect public health.

870   Results of the NACC-CMAQ system during recent late summer (September 2020) and

871   winter (January 2021) months show significant changes in both meteorological and chemical

872   predictions compared to the prior NAQFC. The GFSv16 for NACC-CMAQ has a persistently

873   large dry bias (lower Q2) and larger RMSE across much of CONUS in late summer compared to

874   NMMB (i.e., prior NAQFC), which likely stems from excessively dry soil conditions in GFS.

875   GFS is generally cooler in the east and warmer in the west for surface temperature (TEMP2)

876   compared to NMMB, but the overall MB and RMSE are more similar between the models

877   compared to that for Q2. The GFS has a relatively similar planetary boundary layer height

878   (PBLH) at night, but the PBLH in GFSv16 (NACC-CMAQ) is consistently deeper during the

879   daytime peak hours compared to the prior NAQFC.

880   The differences in surface characteristics, meteorology, and both anthropogenic and natural

881   emissions are driving factors for distinct atmospheric composition differences, where NACC-

882   CMAQ generally outperforms the prior NAQFC for both hourly O_3 and $PM_{2.5}$, especially with

883   improved correlation (R) and IOA. This agrees well with significant improvements in the

884   diurnal O_3 and $PM_{2.5}$ patterns for NACC-CMAQ, with distinct improvements in the day-to-night

885   O_3 slope/cutoff. While overall similar, the maximum daily 8-hr average (MDA8) O_3 is

886   predominantly higher for NACC-CMAQ compared to prior NAQFC, which leads to some

887   forecast degradation due to larger overpredictions of the daytime max O_3.

888   The NACC-CMAQ model became the next operational version of the NAQFC at

889   NWS/NOAA on July 20, 2021, and is available on GitHub for continuous integration, future

890   code updates, and potential community research applications. An ongoing comparison and

891   evaluation of the GFSv16/NACC-CMAQ output with a GFSv16-downscaled Weather Research

892   and Forecasting (WRF) Version 4 (Skamarock et al., 2019) and CMAQ application will

893   highlight the potential of NACC-CMAQ to serve as an additional community research tool for

894   air quality applications.

895   While there are substantial advancements in NACC-CMAQ compared to the prior

896   NAQFC, challenges and limitations remain. One need is to bridge the gap from using a VIIRS

897   LAI climatology to a rapid-refresh, i.e., dynamic methodology (similar to the GVF method here)

898   in NACC-CMAQ. There is also a need to consider shifting the paradigm from using "big-leaf"

899   (i.e., homogeneous single layer of phytomass) assumptions that strongly affect the biosphere-

900   atmosphere exchange processes pivotal to both meteorological and chemical model predictions

901   (refer to Bonan et al., 2021). Simple multilayer canopies have shown to reduce overpredictions

902   of ground-level surface O_3 in the summer due to photolysis attenuation and modified vertical

903   turbulence (Makar et al., 2017), which have significant implications for the daytime O_3

904   overpredictions in the current and future versions of NAQFC (Figures 14a-b and S26). We are

905   currently working on similar canopy effects in NACC-CMAQ to reduce the summer O_3

906   overpredictions in the east-southeast and parts of western CONUS, where there are relatively

907   continuous vegetation/canopies (Figures 14a-b).   Other advancements that are important to

908   improving the future versions of the NAQFC include dynamically updated (and weather-

909   dependent) anthropogenic emissions sources, and improved treatments of mobile sources (e.g.,

910   Vehicle Induced Turbulence; Makar et al., 2021). Further refinements to the inline windblown

911   dust emissions, wildfire smoke emissions, and other process-based natural emissions sources

912   (e.g. lightning NO) are also needed.

913   Other future directions including migrating the advanced science in the offline 12 km

914   resolution NACC-CMAQ model, to a next-generation inline, high-resolution (e.g., 3 km)

915   modeling framework that fits within NOAA's strategy for the Unified Forecast System (UFS;

916   https://ufscommunity.org/). This model system aims to improve integration of atmospheric

917   composition changes with weather predictions, better resolve finer scale processes, and advance

918   the rapid-refresh techniques for emissions and surface-atmosphere exchange processes. At this

919   time, NACC-CMAQ also does not use dynamic lateral boundary conditions for trace gases, but

920   only has dynamically ingested smoke and dust aerosols at its lateral boundaries from the NOAA

921   operational GEFS-Aerosols model.   Current work is underway to use next-generation UFS-

922   based global model systems as updated lateral boundary conditions for trace gases in the future

923   of the NAQFC.   Development and implementation of the NACC-CMAQ model is an important

924   step to 1) advance the NAQFC closer to the state-of-the-science for regional air quality

925   forecasting, 2) improve community applications of NOAA's FV3GFS-driven atmospheric

926   composition models, and 3) facilitate the future development of inline, regional high-resolution

927   air quality forecasting systems within the UFS framework at NOAA.

928

929

Code and Data Availability

930

931 The NACC code is publicly available at https://doi.org/10.5281/zenodo.5507489 and via

932 GitHub at https://github.com/noaa-oar-arl/NACC.git. The modified version of CMAQv5.3.1

933 used in the advanced NACC-CMAQ model for the next operational NAQFC is available at

934 https://doi.org/10.5281/zenodo.5507511 and via GitHub at https://github.com/noaa-oar-

935 arl/NAQFC.

936 The 0.25 degree FV3-driven Global Forecast System Version 16 data (cycled 4x/day) is

937 available in GRIB2 format at https://www.nco.ncep.noaa.gov/pmb/products/gfs/. The hourly

938 GFSv16 data in gridded NetCDF (~13x13 km globally) format and Gaussian projection that is

939 directly used to drive NACC-CMAQ is also currently being migrated to Amazon Web Services

940 (AWS) Cloud for improved NOAA community air quality research applications. The advanced

941 NACC-CMAQ data, i.e., the current operational NAQFC version as of July 20, 2021, is available

942 for operational (https://airquality.weather.gov/) and interactive

943 (https://digital.mdl.nws.noaa.gov/airquality/#) displays from NWS/NOAA. The official

944 NOAA/EMC verification and diagnostics for the NAQFC system are found at

945 https://www.emc.ncep.noaa.gov/mmb/aq/verification_diagnostics/cmaq_verf/.

Disclaimer

946

947 The scientific results and conclusions, as well as any views or opinions expressed herein,

948 are those of the author(s) and do not necessarily reflect the views of NOAA or the Department of

949 Commerce. The research presented was not funded by EPA and was not subject to EPA's quality

950 system requirements. The views expressed in this article are those of the author(s) and do not

951 necessarily represent the views or the policies of the U.S. Environmental Protection Agency.

952

Author Contribution

Patrick C. Campbell: Conceptualization, Methodology, Software, Data curation, Visualization, Investigation, Writing – original draft. Youhua Tang: Methodology, Software, Data curation, Investigation. Pius Lee: Supervision, Project administration, Funding acquisition. Barry Baker: Methodology, Software, Data curation. Daniel Tong: Methodology, Software, Writing – review & editing, Project administration, Funding acquisition. Rick Saylor: Supervision, Project administration, Funding acquisition, Writing – review & editing. Ariel Stein: Supervision, Project administration, Funding acquisition. Jianping Huang: Software, Data curation. Ho-Chun Huang: Methodology, Software, Data curation. Jeff McQueen: Project administration, Funding acquisition. Li Pan: Software, Data curation. Edward Strobach: Software, Data curation, Writing – review & editing. Ivanka Stajner: Project administration, Funding acquisition. Jamese Sims: Project administration. Jose Tirado-Delgado: Project administration. Youngsun Jung: Project administration, Funding acquisition. Fanglin Yang: Project administration. Tanya Spero: Methodology, Software, Writing – review & editing. Robert Gilliam: Software, Data curation.

Declaration of competing interest

The authors declare that they have no known competing financial interests or personal relationships that could have appeared to influence the work reported in this paper.

Acknowledgments

References

Alexander, B., R.J. Park, D.J. Jacob, and S. Gong (2009). Transition metal-catalyzed oxidation of atmospheric sulfur: global implications for the sulfur budget, *J. Geophys. Res.*, 114, D02309. https://doi.org/10.1029/2008JD010486.

Aligo, E., B.S. Ferrier, E. Rogers, M. Pyle, S.J. Weiss, and I. L. Jirak (2014). Modified microphysics for use in high-resolution NAM forecasts. Proc. 27th Conf. on Severe Local Storms, Madison, WI, Amer. Meteor. Soc., 16A.1. [Available online at https://ams.confex.com/ams/27SLS/webprogram/Paper255732.html.]

American Lung Association. Urban air pollution and health inequities: a workshop report. (2001). *Environ Health Perspect*. 109 Suppl 3(Suppl 3):357-74. PMID: 11427385; PMCID: PMC1240553.

Appel, K. W., R.C. Gilliam, N. Davis, A. Zubrow, and S.C. Howard (2011). Overview of the atmospheric model evaluation tool (amet) v1.1 for evaluating meteorological and air quality models. *Environ. Model. Software*, 26 pp. 434-443. https://doi.org/10.1016/j.envsoft.2010.09.007.

Appel, K. W., J. O. Bash, K. M. Fahey, K. M. Foley, R. C. Gilliam, C. Hogrefe, W. Hutzell et. al. (2021). The Community Multiscale Air Quality (CMAQ) Model Versions 5.3 and 5.3.1: System Updates and Evaluation (2021), *Geosci. Model Dev. Discuss*. https://doi.org/10.5194/gmd-14-2867-2021.

Astitha, M., H. Luo, S.T. Rao, C. Hogrefe, R. Mathur, and N. Kumar (2017). Dynamic evaluation of two decades of WRF-CMAQ ozone simulations over the contiguous United States *Atmos. Environ.*, 164, pp. 102-116. https://doi.org/10.1016/j.atmosenv.2017.05.020.

Bai, L., J. Wang, X. Ma, and H. Lu (2018). Air Pollution Forecasts: An Overview. *Int J Environ Res Public Health*. 15(4): 780. https://doi.org/10.3390/ijerph15040780.

Baker, B. and L. Pan (2017). Overview of the Model and Observation Evaluation Toolkit (MONET) Version 1.0 for Evaluating Atmospheric Transport Models. *Atmosphere*. 8. 11: 210. https://doi.org/10.3390/atmos8110210.

Bash, J. O., J. T. Walker, G. G. Katul, M. R. Jones, E. Nemitz, and W. P. Robarge (2010). Estimation of In-Canopy Ammonia Sources and Sinks in a Fertilized Zea mays Field. *Environ. Sci. Technol.* 44, 1683–1689. https://doi.org/10.1021/es9037269.

Bash, J. O., E. J. Cooter, R. L. Dennis, J. T. Walker, and J. E. Pleim (2013). Evaluation of a regional air-quality model with bidirectional NH3 exchange coupled to an agroecosystem model. *Biogeosciences*, 10(3), 1635–1645. https://doi.org/10.5194/bg-10-1635-2013.

Bash, J.O., K. R. Baker, and M. R. Beaver (2015). Evaluation of improved land use and canopy representation in BEIS v3.61 with biogenic VOC measurements in California. *Geosci. Model Dev. Discuss*. 8, 8117-8154, https://doi.org/10.5194/gmdd-8-8117-2015.

Binkowski, F. S. and S. J. Roselle (2003). Models-3 Community Multiscale Air Quality (CMAQ) model aerosol component 1. Model description. *J. Geophys. Res.*, 108, 4183, https://doi.org/10.1029/2001JD001409.

Binkowski, F. S, S. Arunachalam, Z. Adelman, and J. Pinto (2007). Examining photolysis rates with a prototype on-line photolysis module in CMAQ. *J. Appl. Meteor. and Clim*. 46, 1252-1256. https://doi.org/10.1175/JAM2531.1.

Black (1994). The new NMC meso-scale Eta Model: description and forecast examples. *Weather and Forecasting*. 9, 265-278. https://doi.org/10.1175/1520-0434(1994)009<0265:TNNMEM>2.0.CO;2.

Bonan, G. B., E. G. Patton, J. J. Finnigan, D. D. Baldocchi, and I. N. Harman (2021). Moving beyond the incorrect but useful paradigm: reevaluating big-leaf and multilayer plant canopies to model biosphere-atmosphere fluxes – a review. *Agricultural and Forest Meteorology*. 306. https://doi.org/10.1016/j.agrformet.2021.108435.

Briggs, G. A. (1965). A plume rise model compared with observations. *Journal of the Air Pollution Control Association*. 15 (9), 433-438. https://doi.org/10.1080/00022470.1965.10468404.

Byun, D. W. and J. K. S. Ching, J.K.S. (1999). Science algorithms of the EPA Models-3 Community Multi-scale Air Quality (CMAQ) modeling system, EPA/600/R-99/030, Office of Research and Development, US Environmental Protection Agency.

Byun, D. and K. L. Schere (2006). Review of the governing equations, computational algorithms, and other components of the models-3 community multiscale air quality (CMAQ) modeling system. *Applied Mechanics Reviews*, 59(1–6), 51–77. https://doi.org/10.1115/1.2128636.

Campbell, G. S. and J. M. Norman (1998). An introduction to environmental biophysics, Springer, 5. ISBN : 978-0-387-94937-6.

Campbell, P., Y. Zhang, K. Yahya, K. Wang, C. Hogrefe, G. Pouliot et al. (2015). A Multi-Model Assessment for the 2006 and 2010 Simulations under the Air Quality Model Evaluation International Initiative (AQMEII) Phase 2 over North America: Part I. Indicators of the Sensitivity of O3 and PM2.5 Formation Regimes. *Atmospheric Environment*, 115, 569 – 586, https://doi.org/10.1016/j.atmosenv.2014.12.026.

Campbell, P. C., J. O. Bash, and T. L. Spero (2019). Updates to the Noah land surface model in WRF-CMAQ to improve simulated meteorology, air quality, and deposition. *Journal of Advances in Modeling Earth Systems*, 11, 231–256. https://doi.org/10.1029/2018MS001422

Campbell, P. C., D. Tong, Y. Tang, B. Baker, P. Lee, R. Saylor et al. (2021). Impacts of the COVID-19 Economic Slowdown on Ozone Pollution in the U.S. *Atmospheric Environment*. 264, 118713. https://doi.org/10.1016/j.atmosenv.2021.118713.

Chen, J-H. and S.-J Lin (2011). The remarkable predictability of inter-annual variability of Atlantic hurricanes during the past decade. *Geophysical Research Letters*, 38(L11804):6. https://doi.org/10.1029/2011GL047629.

Chen, J-H. and S.-J Lin (2013). Seasonal predictions of tropical cyclones using a 25-km-resolution general circulation model. *J. Climate*, 26(2):380–398. https://doi.org/10.1175/JCLI-D-12-00061.1.

Chen, F. and J. Dudhia (2001). Coupling an advanced land surface-hydrology model with the Penn State-NCAR MM5 modeling system. Part I: Model implementation and sensitivity. *Monthly Weather Review*, 129(4), 569–585. https://doi.org/10.1175/1520-0493(2001)129<0569:CAALSH>2.0.CO;2.

Chen, X., N. Andronova, B. Van Leer, J.E. Penner, J.P. Boyd, C. Jablonowski, and S. Lin (2013). A Control-Volume Model of the Compressible Euler Equations with a Vertical Lagrangian Coordinate. *Mon. Wea. Rev.,* 141, 2526–2544. https://doi.org/10.1175/MWR-D-12-00129.1

Chen, J-H, S.-J. Lin, L. Zhou, X. Chen, S. L. Rees, M. Bender, and M. Morin (2019). Evaluation of Tropical Cyclone Forecasts in the Next Generation Global Prediction System. *Mon. Wea. Rev*. 3409-3428. https://doi.org/10.1175/MWR-D-18-0227.1.

Chen, X., Y. Zhang, K. Wang, D. Tong, P. Lee, Y. Tang et al. (2021). Evaluation of the offline-coupled GFSv15-FV3-CMAQv5.0.2 in support of the next-generation National Air Quality Forecast Capability over the contiguous United States. *GMD Discussion*. 14, 3969–3993. https://doi.org/10.5194/gmd-14-3969-2021.

Chin, M., P. Ginoux, S. Kinne, B. N. Holben, B. N. Duncan, R. V. Martin, J. et al. (2002). Tropospheric aerosol optical thickness from the GOCART model and comparisons with satellite and sun photometer measurements. *J. Atmos. Sci*. 59, 461-483. https://doi.org/10.1175/1520-0469(2002)059<0461:TAOTFT>2.0.CO;2.

Chin, M., R. B. Rood, S.-J. Lin, J. F. Muller, and A. M. Thomspon (2000). Atmospheric sulfur cycle in the global model GOCART: Model description and global properties. *J. Geophys. Res.* 105, 24,671-24,687. https://doi.org/10.1029/2000JD900384.

Chinese State Council, Air Pollution Prevention and Control Action Plan (Guo Fa [2013] No. 37, Sept. 10, 2013), http://www.gov.cn/zwgk/2013-09/12/content_2486773.htm (in Chinese), archived at https://perma.cc/63LS-QXDJ; English translation at http://en.cleanairchina.org/file/loadFile/26.html, archived at https://perma.cc/S5FB-4ECZ.

Clough, S. A., M. W. Shephard, J. E. Mlawer, J. S. Delamere, M. J. Iacono, K. Cady-Pereira, et al. (2005). Atmospheric radiative transfer modeling: A summary of the AER codes. *Journal of Quantitative Spectroscopy & Radiative Transfer*, 91(2), 233–244. https://doi.org/10.1016/j.jqsrt.2004.05.058

Cooter, E. J., J. O. Bash, J. T. Walker, M. R. Jones, and W. Robarge (2010). Estimation of NH3 bi-directional flux from managed agricultural soils. *Atmospheric Environment*, 44(17), 2107–2115. https://doi.org/10.1016/j.atmosenv.2010.02.044.

Cooter, E. J., J. O. Bash, V. Benson, and L. Ran (2012). Linking agricultural crop management and air quality models for regional to national-scale nitrogen assessments. *Biogeosciences*, 9(10), 4023–4035. https://doi.org/10.5194/bg-9-4023-2012.

Demetriou, C. A. and P. Vineis (2015). Carcinogenicity of ambient air pollution: use of biomarkers, lessons learnt and future directions. J. Thorac. Dis. 7(1):67-95. https://doi.org/10.3978/j.issn.2072-1439.2014.12.31.

Ding, H. and Y. Zhu (2018). NDE Vegetation Products System Algorithm Theoretical Basis Document. Version 4.0. NOAA/NESDIS/OSPO. Accessed on February 02, 2021. Available from: https://www.ospo.noaa.gov/Products/documents/GVF_ATBD_V4.0.pdf

Dong, X., J. S. Fu, K. Huang, D. Tong, and G. Zhuang (2016). Model development of dust emission and heterogeneous chemistry within the Community Multiscale Air Quality modeling system and its application over East Asia. *Atmos. Chem. Phys*., 16, 8157-8180. https://doi.org/10.5194/acp-16-8157-2016.

Driemel, A., J. Augustine, K. Behrens, S. Colle, C. Cox, E. Cuevas-Agulló, et al. (2018). Baseline Surface Radiation Network (BSRN): Structure and data description (1992–2017). *Earth System Science Data*, 10(3), 1491–1501. https://doi.org/10.5194/essd-10-1491-2018.

Eder, B., D. Kang, R. Mathur, S. Yu, and K. Schere (2006). An operational evaluation of the Eta-CMAQ air quality forecast model. *Atmospheric Environment*, 40(26), 4894–4905. https://doi.org/10.1016/j.atmosenv.2005.12.062

Eder, B., D. Kang, R. Mathur, J. Pleim, S. Yu, T. Otte, and G. Pouliot. (2009). A performance evaluation of the National Air Quality Forecast Capability for the summer of 2007. *Atmospheric Environment*, 43(14), 2312–2320. https://doi.org/10.1016/j.atmosenv.2009.01.033

Ek, M. B., K. E. Mitchell, Y. Lin, E. Rogers, P. Grunmann, V. Koren, et al. (2003). Implementation of Noah land surface model advances in the National Centers for Environmental Prediction operational mesoscale Eta model. *Journal of Geophysical Research*, 108(D22), 8851. https://doi.org/10.1029/2002JD003296.

Emery, C., Z. Liu, A. G. Russell, M. T. Odman, G. Yarwood, and N. Kumar (2017). Recommendations on statistics and benchmarks to assess photochemical model performance, *Journal of the Air & Waste Management Association*, 67:5, 582-598. https://doi.org/10.1080/10962247.2016.1265027.

Finkelstein, M. M., M. Jerrett, P. DeLuca, N. Finkelstein, D. K. Verma, K. Chapman, and M. R. Sears (2003). Relation between income, air pollution and mortality: A cohort study. *CMAJ*. 169: 397-402.

Ginoux, P., M. Chin, I. Tegen, J. Prospero, B. Holben, O. Dubovik, and S.-J. Lin (2001). Sources and global distributions of dust aerosols simulated with the GOCART model. *J. Geophys. Res*. 106, 20,255-20,273. https://doi.org/10.1029/2000JD000053.

Grell, G. A., J. Dudhia, and D. R. Stauffer (1994). A description of the fifth-generation Penn State/NCAR Mesoscale Model (MM5). NCAR tech. Note NCAR TN-398-1-STR, 117 pp.

Han, J. and H.-L. Pan (2011). Revision of Convection and Vertical Diffusion Schemes in the NCEP Global Forecast System. *Wea. and Forecasting*, 26, 520-533. https://doi.org/10.1175/WAF-D-10-05038.1.

Han, J., W. Wang, Y. C. Kwon, S.-Y. Hong, V. Tallapragada, and F. Yang (2017): Updates in the NCEP GFS Cumulus Convection Schemes with Scale and Aerosol Awareness. *Wea. and Forecasting*, 32, 2005-2017. https://doi.org/10.1175/WAF-D-17-0046.1.

Han, J. and C. S. Bretherton (2019). TKE-Based Moist Eddy-Diffusivity Mass-Flux (EDMF) Parameterization for Vertical Turbulent Mixing. *Weather and Forecasting*, 34(4), 869-886. https://doi.org/10.1175/WAF-D-17-0046.1.

Harris, L.M. and S. Lin (2013). A Two-Way Nested Global-Regional Dynamical Core on the Cubed-Sphere Grid. *Mon. Wea. Rev.*, 141, 283–306, https://doi.org/10.1175/MWR-D-11-00201.1.

Harris, L.M., S. Lin, and C. Tu (2016). High-Resolution Climate Simulations Using GFDL HiRAM with a Stretched Global Grid. *J. Climate*, 29, 4293–4314, https://doi.org/10.1175/JCLI-D-15-0389.1

Hengl, T., J. Mendes de Jesus, G. B. M. Heuvelink, M. Ruiperez Gonzalez, M. Kilibarda, A. Blagotić, et al. (2017). SoilGrids250m: Global gridded soil information based on machine learning. *PLoS ONE*. 12, e0169748. http://dx.doi.org/10.1371/journal.pone.0169748.

Huang, J., J. McQueen, J. Wilczak, I. Djalalova, I. Stajner, P. Shafran, et al. (2017). Improving NOAA NAQFC PM2.5 Predictions with a Bias Correction Approach. *Wea. Forecasting*, 32, 407–421, https://doi.org/10.1175/WAF-D-16-0118.1.

Huang, J., J. McQueen, B. Yang, P. Shafran, H. C. Huang, P. Bhattacharjee et al. (2019). A comparison of global scale FV3 versus regional scale NAM meteorological drivers for regional air quality forecasting. The 100th AGU Fall Meeting, December 9-13, 2019, San Francisco, CA.

Huang, J., J. McQueen, et al. (2018). Development and evaluation of offline coupling of FV3-based GFS with CMAQ at NOAA. The 17th CMAS Conference, October 22-24, 2018, UNC-Chapel Hill, NC.

Huang, M., D. Tong, P. Lee, L. Pan, Y. Tang, I. Stajner et al. (2015). Toward enhanced capability for detecting and predicting dust events in the western United States: The Arizona case study. *Atmos. Chem. Phys.*, 15, 12 595–12 610. https://doi.org/10.5194/acp-15-12595-2015.

Iacono, M. J., J. S. Delamere, E. J. Mlawer, M. W. Shephard, S. A. Clough, and W. B. Collins (2008). Radiative forcing by long-lived greenhouse gases: Calculations with the AER radiative transfer models. *Journal of Geophysical Research*, 113, D13103. https://doi.org/10.1029/2008JD009944

Institute of Medicine. (1999) Toward Environmental Justice: Research, Education, and Health Policy Needs. Washington, DC: National Academy Press. https://doi.org/10.17226/6034.

Janjić, Z. I. (2000). Comments on "Development and evaluation of a convection scheme for use in climate models." *J. Atmos. Sci.*, 57, 3686. https://doi.org/10.1175/1520-0469(2000)057<3686:CODAEO>2.0.CO;2.

Janjić, Z. I., J. P. Gerrity Jr., and S. Nickovic S. (2001), An alternative approach to nonhydrostatic modeling. *Mon. Wea. Rev.*, 129, 1164–1178, https://doi.org/10.1175/1520-0493(2001)129<1164:AAATNM>2.0.CO;2.

Janjic, Z., and R. L. Gall (2012). Scientific documentation of the NCEP nonhydrostatic multiscale model on the B grid (NMMB). Part 1 Dynamics (No. NCAR/TN-489+STR). University Corporation for Atmospheric Research. https://doi.org/10.5065/D6WH2MZX.

Jimenez, P. A., J. Dudhia, J. F. Gonzalez-Rouco, J. Navarro, J. P. Montavez, & E. Garcia-Bustamante (2012). A revised scheme for the WRF surface layer formulation. *Monthly Weather Review*, 140(3), 898–918. https://doi.org/10.1175/MWR-D-11-00056.1.

Kang, D, B. K. Eder, A. F. Stein, G. A. Grell, S.E. Peckham, and J. Mc Henry (2005). The New England Air Quality Forecasting Pilot Program: Development of an Evaluation Protocol and Performance Benchmark. *Journal of the Air and Waste Management Association*, 55(12), 1782–1796. https://doi.org/10.1080/10473289.2005.10464775.

Karamchandani, P., Y. Long, G. Pirovano, A. Balzarini, and G. Yarwood (2017). Source-sector contributions to European ozone and fine PM in 2010 using AQMEII modeling data. *Atmos. Chem. Phys.*, 17, 5643–5664, https://doi.org/10.5194/acp-17-5643-2017.

Kar Kurt, O., J. Zhang, K. E. and Pinkerton. (2016) Pulmonary Health Effects of Air Pollution. *Curr. Opin. Pulm. Med.* 22 (2), 138-143. https://doi.org/10.1097/MCP.0000000000000248.

Kelly, J. T., P. V. Bhave, C. G. Nolte, U. Shankar, and K. M. Foley (2010). Simulating emission and chemical evolution of coarse sea-salt particles in the Community Multiscale Air Quality (CMAQ) model. *Geosci. Model Dev.*, 3, 257–273. https://doi.org/10.5194/gmd-3-257-2010.

Kim, Y., K. Sartelet, and C. Seigneur (2011a). Formation of secondary aerosols: impact of the gas-phase chemical mechanism. *Atmos. Chem. Phys*. 11, 583e598. http://dx.doi.org/10.5194/acp-11-583-2011.

Kim, Y., F. Couvidat, K. Sartelet, and C. Seigneur (2011b). Comparison of different gas phase mechanisms and aerosol modules for simulating particulate matter formation. *J. Air Waste Manag. Assoc*. 61, 1218e1226. http://dx.doi.org/10.1080/10473289.2011.603999.

Keller, C. A. and M. J. Evans (2019). Application of random forest regression to the calculation of gas-phase chemistry within the GEOS-Chem chemistry model v10. *Geosci. Model Dev.*, 12, 1209–1225, https://doi.org/10.5194/gmd-12-1209-2019.

Krueger, S. K., Q. Fu, K. N. Liou, and H-N. S. Chin (1995). Improvement of an ice-phase microphysics parameterization for use in numerical simulations of tropical convection. *Journal of Applied Meteorology*, 34:281–287. https://doi.org/10.1175/1520-0450-34.1.281.

Landrigan, P. J., R. Fuller, N. J. Acosta, O. Adeyi, R. Arnold, N. Basu et al. (2018). The Lancet Commission on pollution and health. *Lancet.* 391: 462-512. http://dx.doi.org/10.1016/S0140-6736(17)32345-0

Lee, B.-J., B. Kim, and K. Lee (2014). Air Pollution Exposure and Cardiovascular Disease. *Toxicol Res*., 30(2), 71-75. https://doi.org/10.5487/TR.2014.30.2.071,

Lee, P., J. McQueen, I. Stajner, J. Huang, L. Pan, D. Tong, et al. (2017). NAQFC Developmental Forecast Guidance for Fine Particulate Matter (PM 2.5). *Weather and Forecasting*, 32(1), 343–360. https://doi.org/10.1175/waf-d-15-0163.1

Lin, S., 2004: A "Vertically Lagrangian" Finite-Volume Dynamical Core for Global Models. *Mon. Wea. Rev.*, 132, 2293–2307. https://doi.org/10.1175/1520-0493(2004)132<2293:AVLFDC>2.0.CO;2.

Lin, S. and R.B. Rood (1996). Multidimensional Flux-Form Semi-Lagrangian Transport Schemes. *Mon. Wea. Rev.*, 124, 2046–2070. https://doi.org/10.1175/1520-0493(1996)124<2046:MFFSLT>2.0.CO;2.

Lin, Y.-L., R. D. Farley, and H. D. Orville (1983). Bulk parameterization of the snow field in a cloud model. *J. Climate Appl. Meteor.*, 22:1065–1092. https://doi.org/10.1175/1520-0450(1983)022<1065:BPOTSF>2.0.CO;2.

Lin, S., W.C. Chao, Y.C. Sud, and G.K. Walker (1994). A Class of the van Leer-type Transport Schemes and Its Application to the Moisture Transport in a General Circulation Model. *Mon. Wea. Rev.*, 122, 1575–1593. https://doi.org/10.1175/1520-0493(1994)122<1575:ACOTVL>2.0.CO;2

Liu, Y. and T. Wang (2020). Worsening urban ozone pollution in China from 2013 to 2017 – Part 1: The complex and varying roles of meteorology. *Atmos. Chem. Phys.*, 20, 6305–6321, https://doi.org/10.5194/acp-20-6305-2020.

Lord, S. J., H. E. Willoughby, and J. M. Piotrowicz (1984). Role of a parameterized ice-phase microphysics in an axisymmetric, nonhydrostatic tropical cyclone model. *J. Atmos. Sci.*. 41(19):2836–2848. https://doi.org/10.1175/1520-0469(1984)041<2836:ROAPIP>2.0.CO;2.

Makar, P., R. Staebler, A. Akingunola, J. Zhang, C. McLinden, S. K. Kharol, et al. (2017). The effects of forest canopy shading and turbulence on boundary layer ozone. *Nat Commun*. 8, 15243. https://doi.org/10.1038/ncomms15243.

Makar, P. A., C. Stroud, A. Akingunola, J. Zhang, S. Ren, P. Cheung, and Q. Zheng (2021). Vehicle-induced turbulence and atmospheric pollution. *Atmos. Chem. Phys.*, 21, 12291–12316, https://doi.org/10.5194/acp-21-12291-2021.

Marlier, M. E., A. S. Jina, P. L. Kinney, and R. S. DeFries (2016). Extreme Air Pollution in Global Megacities. *Curr Clim Change Rep.* 2, 15–27. https://doi.org/10.1007/s40641-016-0032-z.

Martin, R. L. and T.W. Good (1991). Catalyzed oxidation of sulfur dioxide in solution: the iron-manganese synergism. *Atmospheric Environment*. 25A, 2395-2399. https://doi.org/10.1016/0960-1686(91)90113-L.

Massad, R.-S., E. Nemitz, and M. A. Sutton (2010). Review and parameterization of bi-directional ammonia exchange between vegetation and the atmosphere. *Atmos. Chem. Phys.*, 10, 10359-10386. https://doi.org/10.5194/acp-10-10359-2010.

Mathur, R., S. Yu, D. Kang, and K. L. Schere (2008). Assessment of the wintertime performance of developmental particulate matter forecasts with the Eta-Community Multiscale Air Quality modeling system. *Journal of Geophysical Research*, 113(D2), D02303. https://doi.org/10.1029/2007JD008580

Matthias, V., J. A. Arndt, A, Aulinger, J. Bieser, H. Denier van der Gon, R. Kranenburg, et al. (2018) Modeling emissions for three-dimensional atmospheric chemistry transport models. *Journal of the Air & Waste Management Association*, 68:8, 763-800, DOI: https://doi.org/10.1080/10962247.2018.1424057.

McKeen, S., J. Wilczak, G. Grell, I. Djalova, S. Peckham, E.-Y. Hsie, et al. (2005). Assessment of an ensemble of seven real-time ozone forecasts over eastern North America during the summer of 2004. *J. Geophys. Res*. 110, D21307. http://dx.doi.org/10.1029/2005JD005858.

McKeen, S., S. H. Chung, J. Wilczak, G. Grell, I. Djalalova, S. Peckham, W. Gong, V. Bouchet, R. Moffet, Y. Tang, G. R. Carmichael, R. Mathur, S. Yu (2007). Evaluation of several PM2.5 forecast models using data collected during the ICARTT/NEAQS 2004 field study. *J. Geophys. Res*. 112, D10S20. http://dx.doi.org/10.1029/2006JD007608.

McKeen, S., G. Grell, S. Peckham, J. Wilczak, I. Djalalova, E. Hsie, et al. (2009). An evaluation of real-time air quality forecasts and their urban emissions over eastern Texas during the summer of 2006 Second Texas Air Quality Study field study. *J. Geophys. Res*. 114, D00F11. http://dx.doi.org/10.1029/2008JD011697.

Miller J, H. Safford, M. Crimmins, and A. Thode (2009). Quantitative evidence for increasing forest fire severity in the Sierra Nevada and Southern Cascade Mountains, California and Nevada, USA. *Ecosystems* 12:16–32. https://doi.org/10.1007/s10021-008-9201-9.

Mlawer, E. J., S. J. Taubman, P. D. Brown, M. J. Iacono, and S. A. Clough (1997). Radiative transfer for inhomogeneous atmosphere: RTTM, a validated correlated-k model for the longwave. *J. Geophys. Res*., 102, 16 663–16 682. https://doi.org/10.1029/97JD00237.

Monin, A. S., and A. M. Obukhov (1954). Basic laws of turbulent mixing in the surface layer of the atmosphere (in Russian). *Tr. Akad. Nauk SSSR Geophiz. Inst.* 24(151), 151, 163–187.

Myneni, R., and Y. Knyazikhin (2018). VIIRS/NPP Leaf Area Index/FPAR 8-Day L4 Global 500m SIN Grid V001 [Data set]. NASA EOSDIS Land Processes DAAC. Accessed 2021-02-22 from https://doi.org/10.5067/VIIRS/VNP15A2H.001.

National Emissions Inventory (NEI). (2014). [Data set]. Retrieved February 26, 2020, from https://edap.epa.gov/public/extensions/nei_report_2014/dashboard.html#sector-db.

National Emissions Inventory Collaborative (2019). [Data set]. 2016v1 Emissions Modeling Platform. Retrieved from http://views.cira.colostate.edu/wiki/wiki/10202.

Nemitz, E., M. A. Sutton, J. K. Schjoerring, S. Husted, and G. P. Wyers. (2000). Resistance modelling of ammonia exchange over oilseed rape. *Agricultural and Forest Meteorology*. 105(4). 405–425. https://doi.org/10.1016/S0168-1923(00)00206-9.

Niinemets, Ü., A. Arneth, U. Kuhn, R. K. Monson, J. Peñuelas, and M. Staudt (2010). The emission factor of volatile isoprenoids: stress, acclimation, and developmental responses. *Biogeosciences*. 7, 2203–2223. https://doi.org/10.5194/bg-7-2203-2010.

O'Neill M. S., M. Jerrett, I. Kawachi, J. I. Levy, A. J. Cohen, N. Gouveia, et al. (2003). Health, wealth, and air pollution: Advancing theory and methods. *Environ Health Perspect*. 111: 1861-1870. https://doi.org/10.1289/ehp.6334.

O'Neill, S. M., N. K. Larkin, J. Hoadley, G. Mills, J. K. Vaughan, R. R. Draxler, et al. (2009). Regional real-time smoke prediction systems. Wildland Fires and Air Pollution, A. Bytnerowicz et al., Eds., Developments in Environmental Science, Vol. 8, Elsevier, 499–534.

Otte, T. L., and J. E. Pleim (2010). The Meteorology-Chemistry Interface Processor (MCIP) for the CMAQ modeling system: updates through MCIPv3.4.1. *Geosci. Model Dev*., 3, 243–256, https://doi.org/10.5194/gmd-3-243-2010.

Otte, T. L., Pouliot, G., Pleim, J. E., Young, J. O., Schere, K. L., Wong, D. C., et al. (2005). Linking the Eta Model with the Community Multiscale Air Quality (CMAQ) Modeling System to Build a National Air Quality Forecasting System. Weather and Forecasting, 20(3), 367–384. https://doi.org/10.1175/WAF855.1

Pan, L., H. Kim, P. Lee, R. Saylor, Y. Tang, D. Tong, et. al. (2020). Evaluating a fire smoke simulation algorithm in the National Air Quality Forecast Capability (NAQFC) by using multiple observation data sets during the Southeast Nexus (SENEX) field campaign. *Geosci. Model Dev*., 13, 2169–2184. https://doi.org/10.5194/gmd-13-2169-2020.

Pinder, R.W., R. L. Dennis, and P. V. Bhave (2008). Observable indicators of the sensitivity of PM2.5 nitrate to emission reductions: part I. Derivation of the adjusted gas ratio and applicability at regulatory-relevant time scales. *Atmos. Environ*. 42 (6), 1275e1286. https://doi.org/10.1016/j.atmosenv.2007.10.039.

Pleim, J. E. (2007a). A combined local and nonlocal closure model for the atmospheric boundary layer. Part I: Model description and testing. *J. Appl. Meteor. Climatol*. 46, 1383–1395, https://doi.org/10.1175/JAM2539.1.

Pleim, J. E. (2007b). A combined local and nonlocal closure model for the atmospheric boundary layer. Part II: Application and evaluation in a mesoscale meteorological model. *J. Appl. Meteor*. Climatol. 46, 1396–1409. https://doi.org/10.1175/JAM2534.1.

Pleim, J., and L. Ran (2011). Surface flux modeling for air quality applications. *Atmosphere*, 2(3), 271–302. https://doi.org/10.3390/atmos2030271.

Pleim, J. E., J. O. Bash, J. T. Walker, and E. J. Cooter (2013). Development and evaluation of an ammonia bidirectional flux parameterization for air quality models. *Journal of Geophysical Research: Atmospheres*, 118, 3794–3806. https://doi.org/10.1002/jgrd.50262.

Pleim, J. E., L. Ran, W. Appel, M. W. Shephard, and K. Cady-Pereira (2019). New bidirectional ammonia flux model in an air quality model coupled with an agricultural model. *Journal of Advances in Modeling Earth Systems*, 11, 2934– 2957. https://doi.org/10.1029/2019MS001728.

Powers, J. G., J. B. Klemp, W. C. Skamarock, C. A. Davis, J. Dudhia, D. O. Gill, et al. (2017). The weather research and forecasting model: Overview, system efforts, and future directions. *Bulletin of the American Meteorological Society*, 98(8), 1717–1737. https://doi.org/10.1175/BAMS-D-15-00308.1.

Putman, W. M., and S.-J. Lin (2007). Finite-volume transport on various cubed-sphere grids, *Journal of Computational Physics*. 227, 1, 10, 55-78. https://doi.org/10.1016/j.jcp.2007.07.022

Pye, H. O. T., R. W. Pinder, I. Piletic, Y. Xie, S. L. Capps, Y.-H. Lin, et al. (2013). Epoxide pathways improve model predictions of isoprene markers and reveal key role of acidity in aerosol formation. *Environmental Science & Technology*. https://doi.org/10.1021/es402106h.

Pye, H. O. T., B. N. Murphy, L. Xu, N. L. Ng, A. G. Carlton, H. Guo, et al. (2017). On the implications of aerosol liquid water and phase separation for organic aerosol mass. *Atmospheric Chemistry and Physics*. 17, 343-369. https://doi.org/10.5194/acp-17-343-2017.

Ran, L., E. Cooter, V. Benson, and Q. He (2011). Development of an agricultural fertilizer modeling system for bi-directional ammonia fluxes in the CMAQ model. In D. G. Steyn, & S. T. Castelli (Eds.), Air Pollution Modeling and its Application XXI (Chapter 36, (pp. 213–219). Dordrecht: Springer. https://doi.org/10.1007/978-94-007-1359-8_36.

Ran, L., J. Pleim, R. Gilliam, F. S. Binkowski, C. Hogrefe, and L. Band (2016). Improved meteorology from an updated WRF/CMAQ modeling system with MODIS vegetation and albedo. *J. Geophys. Res. Atmos*. 121, 2393– 2415. https://doi.org/10.1002/2015JD024406.

Rogers, E., T. Black, D. Deaven, G. DiMego, Q. Zhao, M. Baldwin, et al. (1996). Changes to the operational "early" Eta Analysis/Forecast System at the National Centers for Environmental Prediction. *Weather and Forecasting*. 11 391-413. https://doi.org/10.1175/1520-0434(1996)011<0391:CTTOEA>2.0.CO;2.

Ruminski, M, and S. Kondragunta (2006). Monitoring fire and smoke emissions with the hazard mapping system. *Proceedings Volume 6412. Disaster Forewarning Diagnostic Methods and Management*. https://doi.org/10.1117/12.694183.

Ruminski, M., J. Simko, J. Kibler, S. Kondragunta, R. Draxler, P. Davidson, and P. Li (2008). Use of multiple satellite sensors in NOAA's operational near real-time fire and smoke detection and characterization program. *Remote Sensing of Fire: Science and Applicatio*n. https://doi.org/10.1117/12.807507.

Sarwar, G., K. Fahey, S. Napelenok, S. Roselle, and R. Mathur (2011). Examining the impact of CMAQ model updates on aerosol sulfate predictions. The 10th Annual CMAS Models-3 User's Conference, October, Chapel Hill, NC.

Sarwar, G., B. Gantt, K. Foley, K. Fahey, T. L. Spero, D. Kang, et al. (2019). Influence of bromine and iodine chemistry on annual, seasonal, diurnal, and background ozone: CMAQ

simulations over the Northern Hemisphere. *Atmospheric Environment*. 213. 395-404. https://doi.org/10.1016/j.atmosenv.2019.06.020.

Schwede, D., G. A. Pouliot, and T. Pierce (2005). Changes to the Biogenic Emissions Inventory System Version 3 (BEIS3). In Proceedings of the 4th CMAS Models-3 Users' Conference, Chapel Hill, NC, 26–28 September 2005.

Schroeder, W., M. Ruminski, I. Csiszar, L. Giglio, E. Prins, C. Schmidt, and Morisette, J. (2008). Validation analyses of an operational fire monitoring product: The Hazard Mapping System, *Int. J. Remote Sens*., 29, 6059–6066. https://doi.org/10.1080/01431160802235845.

Sillman, S. (1995). The use of NOy, H2O2, and HNO3 as indicators for ozone-NOx-hydrocarbon sensitivity in urban locations. *J. Geophys. Res. Atmos*. 100, 14175–14188. http://doi.wiley.com/10.1029/94JD02953.

Sillman, S., The relation between ozone, NOx and hydrocarbons in urban and polluted rural environments. *Atmos. Environ*., 33, 12, 1821-1845. https://doi.org/10.1016/S1352-2310(98)00345-8.

Sillman, S., J. A. Logan, and S. C. Wofsy (1990). The sensitivity of ozone to nitrogen oxides and hydrocarbons in regional ozone episodes. *J. Geophys. Res*. 95, 1837–1852. https://doi.org/10.1029/JD095iD02p01837.

Skamarock, W. C., and J. B. Klemp (2008). A time-split nonhydrostatic atmospheric model for weather research and forecasting applications. *Journal of Computational Physics*. 227(7), 3465–3485. https://doi.org/10.1016/j.jcp.2007.01.037.

Skamarock, W. C., J. B. Klemp, J. Dudhia, D. O. Gill, Z. Liu, J. Berner, and X. Huang (2019). A Description of the Advanced Research WRF Model Version 4 (No. NCAR/TN-556+STR). https://doi.org/10.5065/1dfh-6p97.

Sofiev, M., T. Ermakova, and R. Vankevich (2012). Evaluation of the smoke-injection height from wild-land fires using remote-sensing data. *Atmos. Chem. Phys*.. 12, 1995–2006, https://doi.org/10.5194/acp-12-1995-2012.

Stajner, I., P. Davidson, D. Byun, J. McQueen, R. Draxler, P. Dickerson, and J. Meagher (2011). US National Air Quality Forecast Capability: Expanding Coverage to Include Particulate Matter (pp. 379–384). Springer, Dordrecht. https://doi.org/10.1007/978-94-007-1359-8_64.

Sun, J., J. S. Fu, K. Huang, and Y. Gao (2015). Estimation of future PM2.5- and ozone-related mortality over the continental United States in a changing climate: An application of high-resolution dynamical downscaling technique, *Journal of the Air & Waste Management Association.* 65:5, 611-623, https://doi.org/10.1080/10962247.2015.1033068.

Tang, Y., P. Lee, M. Tsidulko, H.-C. Huang, J. Mcqueen, G. DiMego, et al. (2009). The impact of chemical lateral boundary conditions on CMAQ predictions of tropospheric ozone over the

continental United States. *Environmental Fluid Mechanics*. 9. 43-58. https://doi.org/10.1016/10.1007/s10652-008-9092-5.

Tang, Y., T. Chai, L. Pan, P. Lee, D. Tong, H.-C. Kim, and W. Chen (2015). Using optimal interpolation to assimilate surface measurements and satellite AOD for ozone and PM2.5: A case study for July 2011. *Journal of the Air & Waste Management Association.* 65:10, 1206-1216, https://doi.org/10.1080/10962247.2015.1062439.

Tang, Y., H. Bian, Z. Tao, L. D. Oman, D. Tong, P. Lee, et al. (2021). Comparison of chemical lateral boundary conditions for air quality predictions over the contiguous United States during pollutant intrusion events. *Atmos. Chem. Phys*. 21, 2527–2550. https://doi.org/10.5194/acp-21-2527-2021.

Tewari, M., F. Chen, W. Wang, J. Dudhia, M. A. LeMone, K. Mitchell, et al. (2004). Implementation and verification of the unified NOAH land surface model in the WRF model. Paper Presented at the 20th Conference on Weather Analysis and Forecasting/16th Conference on Numerical Weather Prediction, Seattle, WA.

Tong, D. Q., P. Lee, and R.D. Saylor (2012). New Direction: The need to develop process-based emission forecasting models, *Atmospheric Environment*, 47: 560-561. https://doi.org/10.1016/j.atmosenv.2011.10.070.

Tong, D. Q., J. X. L. Wang, T. E. Gill, H. Lei, and B. Wang (2017). Intensified dust storm activity and Valley fever infection in the southwestern United States. *Geophys. Res. Lett*., 44, 4304– 4312. https://doi.org/10.1016/10.1002/2017GL073524.

Troen, I., and L. Mahrt (1986). A simple model of the atmospheric boundary layer: Sensitivity to surface evaporation. *Bound.-Layer Meteor*., 37, 129–148. https://doi.org/10.1007/BF00122760.

US EPA Office of Research and Development. (2014). CMAQv5.0.2 (Version 5.0.2). Zenodo. http://doi.org/10.5281/zenodo.1079898.

US EPA Office of Research and Development. (2019). CMAQ (Version 5.3.1). Zenodo. http://doi.org/10.5281/zenodo.3585898.

Vukovich, J. M., and T. Pierce (2002). The Implementation of BEIS3 within the SMOKE modeling framework. *Environmental Science.*

Weiss, A. and J. Norman (1985). Partitioning solar radiation into direct and diffuse, visible and nearinfrared components. *Agr. Forest Meteorol*., 34, 205–213. https://doi.org/10.1016/0168-1923(85)90020-6.

Westerling A. L., H. G. Hidalgo, D. R. Cayan, and T. W. Swetnam (2006). Warming and earlier spring increase western US forest wildfire activity. *Science*. 313:940–943. https://doi.org/10.1126/science.1128834.

Wilkins, J., G. Pouliot, T. Pierce, and J. Beidler (2019). Exploring the Vertical Distribution of Wildland Fire Smoke in CMAQ. 2019 International Emissions Inventory Conference, Dallas, Texas, July 28 - August 02, 2019.

Williams, J. R. (1995). The EPIC model. In V. P. Singh (Ed.), Computer models in watershed hydrology (Chapter 25, (pp. 909–1000). Littleton, CO: Water Resources Publications.

Williams, A. P., E. R. Cook, J. E. Smerdon, B. I. Cook, J. T. Abatzoglou, K. Bolles, et al. (2020). Large contribution from anthropogenic warming to an emerging North American megadrought. *Science*. 368, 314-318. https://doi.org/10.1126/science.aaz9600.

World Health Organization (WHO) (2006). Air Quality Guidelines. Global update 2005. Particulate matter, ozone, nitrogen dioxide and sulfur dioxide. ISBN: 92-890-2192-6.

World Health Organization (WHO) (2010). WHO Guidelines for Indoor Air Quality: Selected Pollutants. World Health Organization, Regional Office for Europe Scherfigsvej 8, DK-2100 Copenhagen Ø, Denmark, ISBN 9789289002134.

Yang, F., V. Tallapragada, J. S. Kain, H. Wei, R. Yang, V. A. Yudin, et al. (2020). Model Upgrade Plan and Initial Results from a Prototype NCEP Global Forecast System Version 16. 2020 AMS Conference, Boston, MA. https://ams.confex.com/ams/2020Annual/webprogram/Paper362797.html

Yarwood, G., S. Rao, M. Yocke, and G. Whitten (2005). Updates to the carbon bond chemical mechanism: CB05. Final Rep. to the US EPA, RT-0400675. [Available online at http://www.camx.com/publ/pdfs/cb05_final_report_120805.pdf.]

Yarwood, G., G. Z. Whitten, and J. Jung (2010). Final Report. Development, Evaluation and Testing of Version 6 of the Carbon Bond Chemical Mechanism (CB6). ENVIRON International Corporation. 06-17477Y. September 22, 2010.

Zeka A., A. Zanobetti, and J. Schwartz (2006). Short term effects of particulate matter on cause specific mortality: effects of lags and modification by city characteristics. *Occup Environ Med*. 62: 718-725. https://doi.org/10.1136/oem.2004.017012.

Zhang, X., S. Kondragunta, J. Ram, C. Schmidt, and H.-C. Huang (2012). Near-real-time global biomass burning emissions product from geostationary satellite constellation. *Journal of Geophysical Research: Atmospheres*, 117(D14). https://doi.org/10.1029/2012JD017459.

Zhang, X., S. Kondragunta, and D. P. Roy (2014). Interannual variation in biomass burning and fire seasonality derived from geostationary satellite data across the contiguous United States from 1995 to 2011. *Journal of Geophysical Research: Biogeosciences*. 119(6), 1147–1162. https://doi.org/10.1002/2013JG002518.

Zhang, Y., K. Vijayaraghavan, X.-Y. Wen, H. E. Snell, and M. Z. Jacobson, M.Z. (2009a.) Probing into regional ozone and particulate matter pollution in the United States: 1. A 1 year CMAQ simulation and evaluation using surface and satellite data. *J. Geophys. Res*. 114, D22304. https://doi.org/10.1029/2009JD011898.

Zhang, Y., X.-Y. Wen, K. Wang, K. Vijayaraghavan, and M. Z. Jacobson (2009b). Probing into regional ozone and particulate matter pollution in the United States: 2. An examination of formation mechanisms through a process analysis technique and sensitivity study. *J. Geophys. Res*. 114. https://doi.org/10.1029/2009JD011898.

Zhang, Y., M. Bocquet, V. Mallet, C. Seigneur, and A. Baklanov. (2012a). Real-time air quality forecasting, part I: History, techniques, and current status. *Atmospheric Environment*. 60, 632-655. https://doi.org/10.1016/j.atmosenv.2012.06.031.

Zhang, Y., M. Bocquet, V. Mallet, C. Seigneur, and A. Baklanov, A. (2012b). Real-time air quality forecasting, part II: State of the science, current research needs, and future prospects. *Atmospheric Environment*. 60, 656-676. https://doi.org/10.1016/j.atmosenv.2012.02.041.

Zhang, Y., J. J. West, R. Mathur, J. Xing, C. Hogrefe, S. J. Roselle, et al. (2018) Long-term trends in the ambient PM2.5- and O3-related mortality burdens in the United States under emission reductions from 1990 to 2010. *Atmos. Chem. Phys*., 18, 15003–15016, https://doi.org/10.5194/acp-18-15003-2018.

Zhao, H., Y. Zheng, and T. Li (2017). Air Quality and Control Measures Evaluation during the 2014 Youth Olympic Games in Nanjing and its Surrounding Cities. *Atmosphere*. 8, 100. https://doi.org/10.3390/atmos8060100.

Zhou, L., S. Lin, J. Chen, L.M. Harris, X. Chen, and S.L. Rees (2019). Toward Convective-Scale Prediction within the Next Generation Global Prediction System. *Bull. Amer. Meteor. Soc*., 100, 1225–1243. https://doi.org/10.1175/BAMS-D-17-0246.1.

Zhou, T., J. Sun, and H. Yu (2017). Temporal and Spatial Patterns of China's Main Air Pollutants: Years 2014 and 2015. *Atmosphere* 8, 137. https://doi.org/10.3390/atmos8080137.